

Astroparticle Physics

2019/20

Lectures:

04.02.2020 [1. Historical introduction, basic properties of cosmic rays](#)

06.02.2020 [2. Hadronic interactions and accelerator data](#)

11.02.2020 [3. Cascade equations](#)

13.02.2020 [4. Electromagnetic cascades](#)

18.02.2020 [5. Extensive air showers](#)

20.02.2020 6. Detectors for extensive air showers

27.02.2020 7. High energy cosmic rays and the knee in the energy spectrum of cosmic rays

03.03.2020 8. Radio detection of extensive air showers

05.03.2020 9. Acceleration, astrophysical accelerators and beam dumps

10.03.2020 10. Extragalactic propagation of cosmic rays

12.03.2020 11. Ultra high energy cosmic rays

17.03.2020 12. Astrophysical gamma rays and neutrinos

14.04.2020 13. Neutrino astronomy

12.05.2020 14. Gamma-ray astronomy

<http://particle.astro.ru.nl/goto.html?astropart1920>

lecture 5

Extensive air showers

Gaisser chapter 16

16 Extensive air showers

- 16.1 Basic features of air showers
- 16.2 The Heitler–Matthews splitting model
- 16.3 Muons in air showers
- 16.4 Nuclei and the superposition model
- 16.5 Elongation rate theorem
- 16.6 Shower universality and cross section measurement
- 16.7 Particle detector arrays
- 16.8 Atmospheric Cherenkov light detectors
- 16.9 Fluorescence telescopes
- 16.10 Radio signal detection

Extensive Air Shower

Proton 10^{15} eV:

on ground

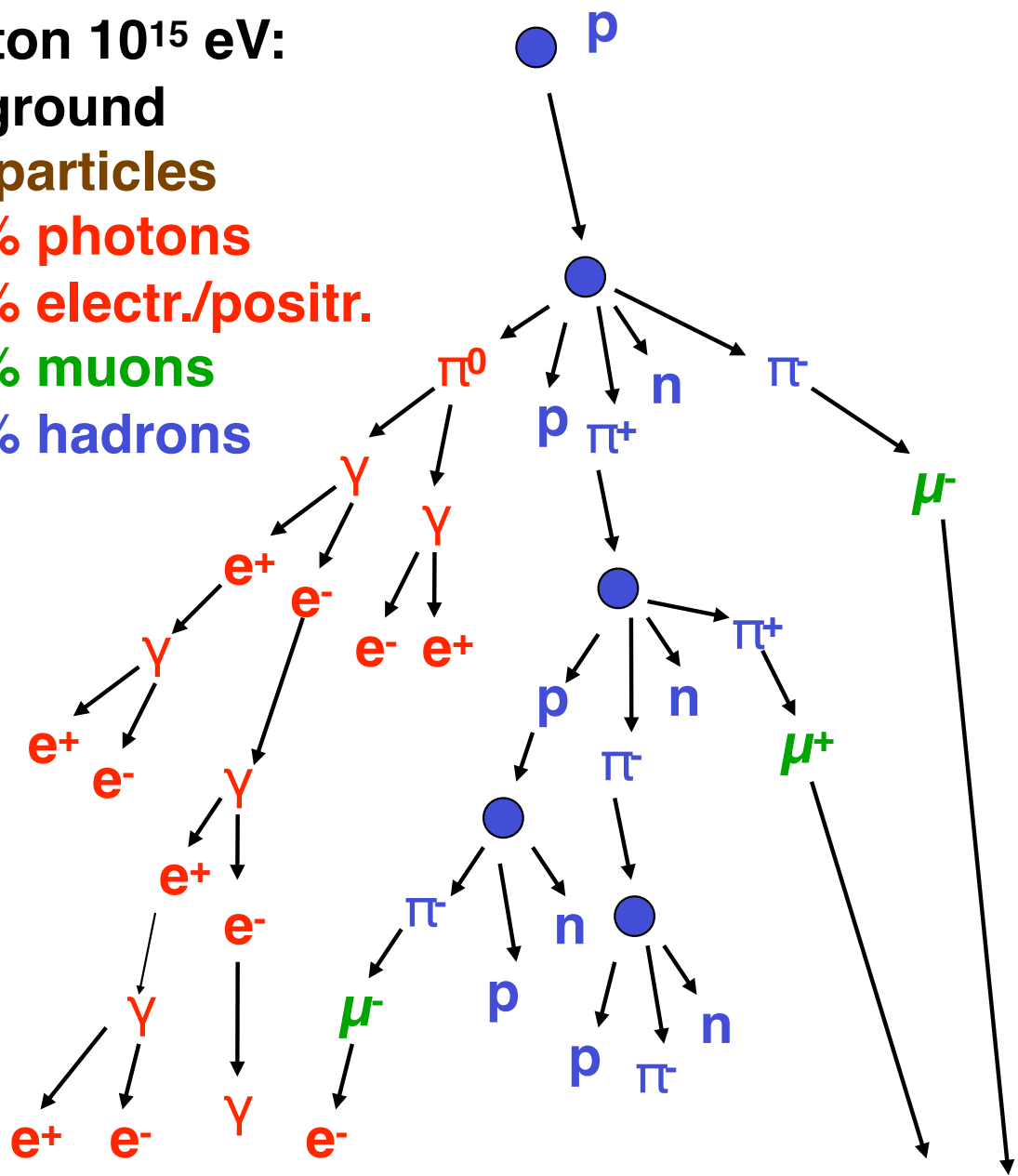
10^6 particles

80% photons

18% electr./positr.

1.7% muons

0.3% hadrons

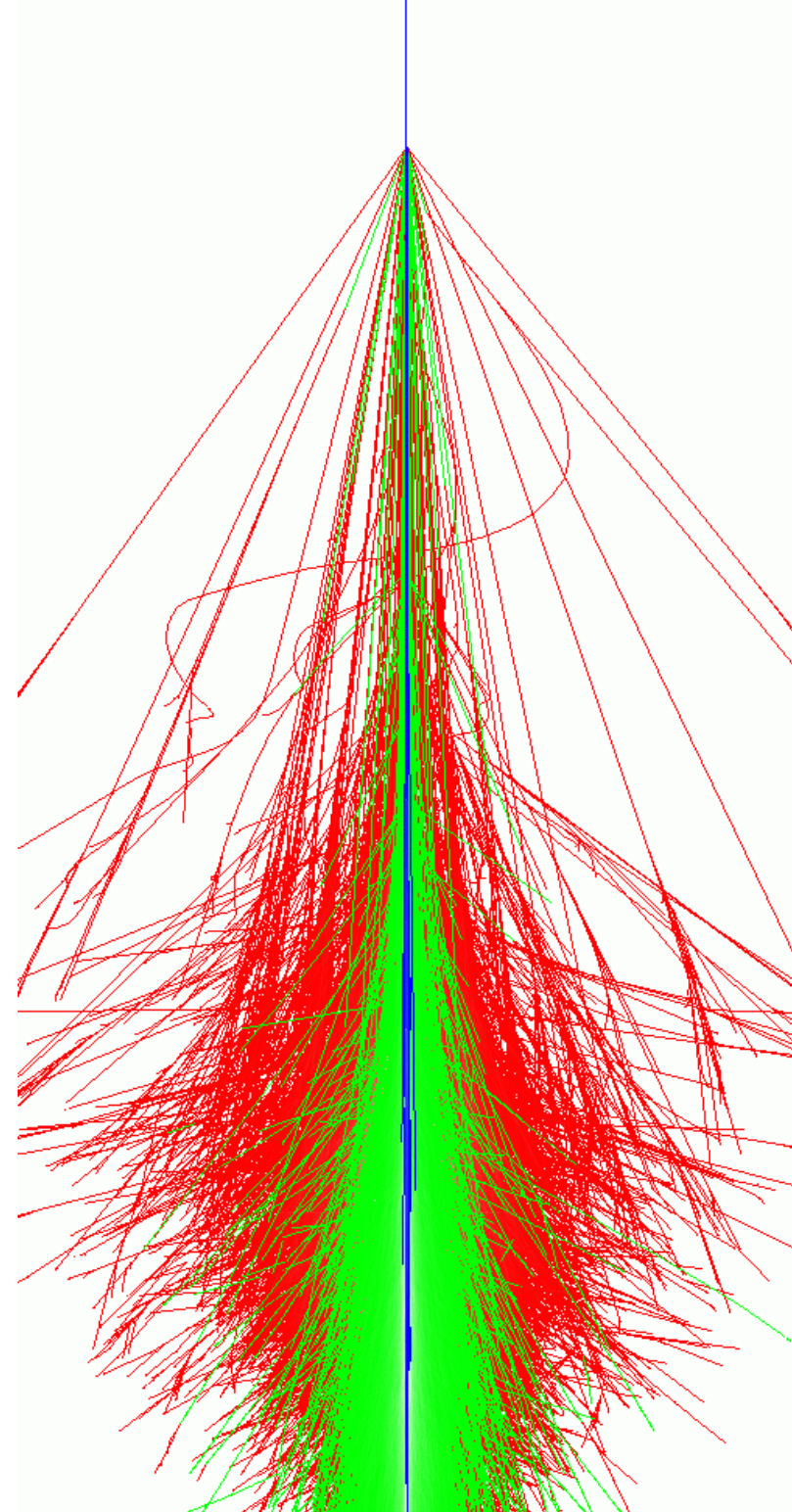


electromagnetic

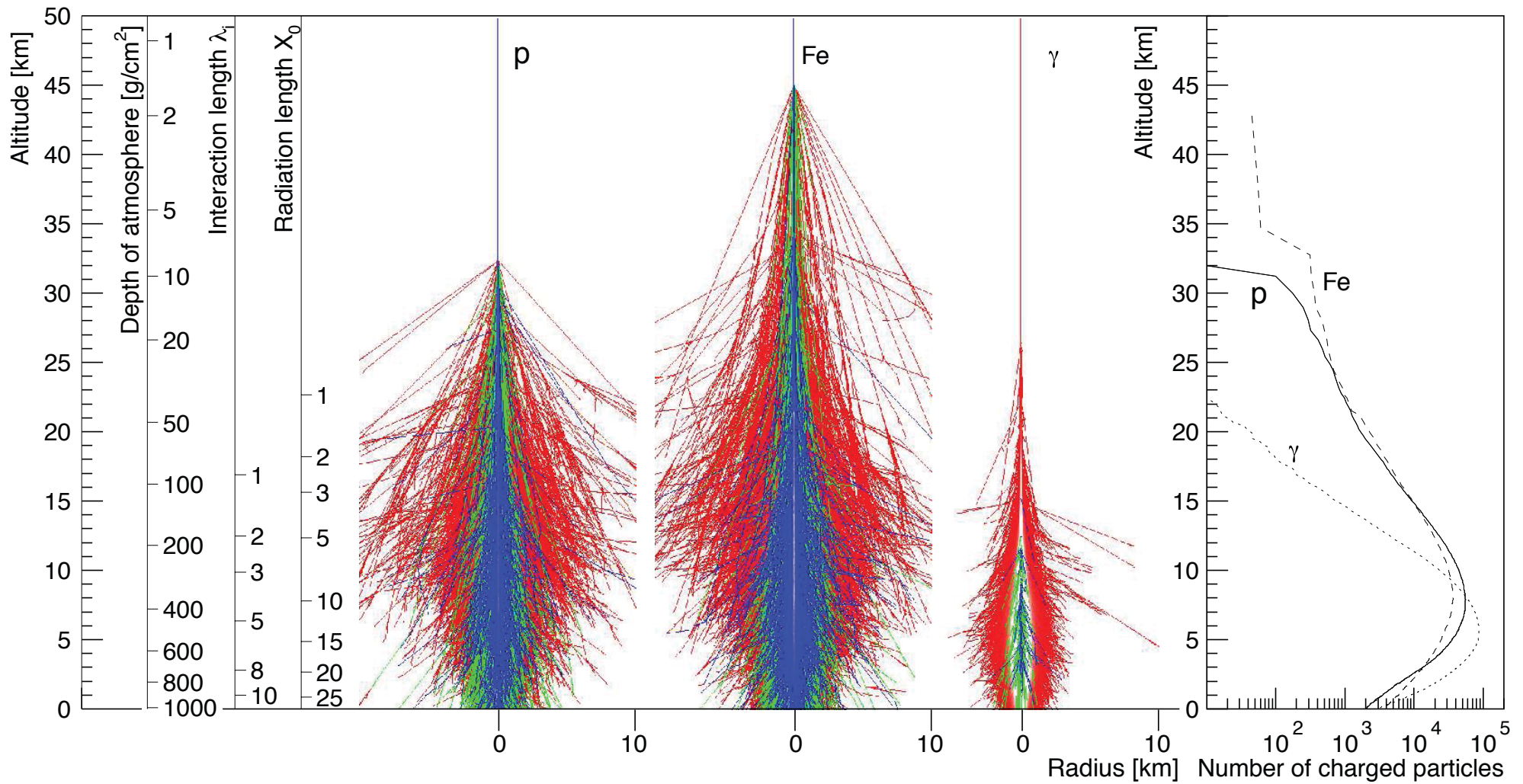
hadronic

muonic

shower component



examples of showers with same (total) energy



16.1 Basic features of air showers

At each hadronic interaction, slightly more than a third of the energy goes into the electromagnetic component. Since most hadrons re-interact, most of the primary energy eventually finds its way into the electromagnetic component. In addition, because of the rapid multiplication of electromagnetic cascades, electrons and positrons are the most numerous charged particles in cosmic ray air showers. Thus, most of the shower energy is eventually dissipated by ionization losses of the electrons and positrons. It is correct to think of the atmosphere as a calorimeter to be sampled by the air shower detector. Apart from the small fraction, $F(E_0)$, of energy lost to neutrinos, the primary energy, E_0 is given by the *track length integral*,

$$(1 - F) \times E_0 \sim \alpha \times \int_0^\infty dX N(X), \quad (16.1)$$

where $N(X)$ is the number of charged particles in the shower at depth X (measured along the shower axis) and α is the energy loss per unit path length in the atmosphere averaged over all electron energies ($\alpha \approx 2.5 \text{ MeV}/(\text{g}/\text{cm}^2)$). In practice the track length integral must be extrapolated beyond the slant depth at the ground to account for energy remaining in the shower when it reaches the surface.

Energy measurement - calorimeter

hadron calorimeter

longitudinal shower development

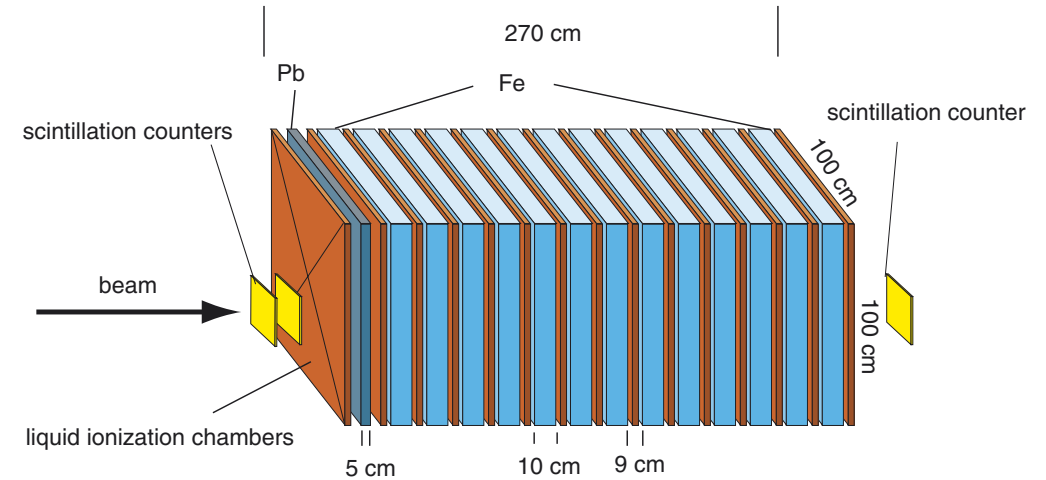


Fig. 2. Schematic view of the sampling calorimeter.

S. Plewnia et al. / Nuclear Instruments and Methods in Physics Research A 566 (2006) 422–432

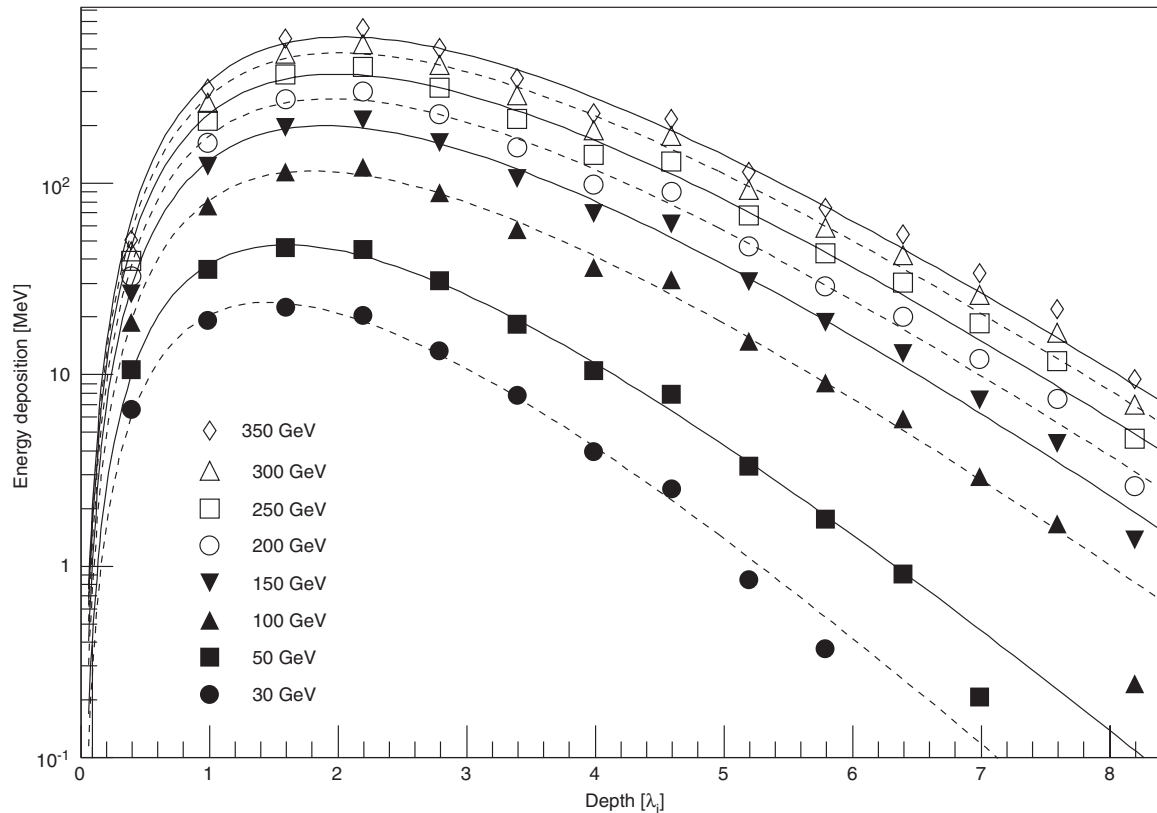


Fig. 13. Measured energy deposition as function of depth in the calorimeter for hadrons with energies from 30 to 350 GeV. The lines represent fits according to Eq. (7).

sampling calorimeter
alternating layers of absorber material and detectors

energy resolution

$$\frac{\sigma(e)}{E} = A + B \frac{1}{\sqrt{E}}$$

$$E_{\text{dep}}(t) = A \cdot t^B \cdot \exp(-t/C)$$

Energy measurement - calorimeter

hadron calorimeter

lateral shower development

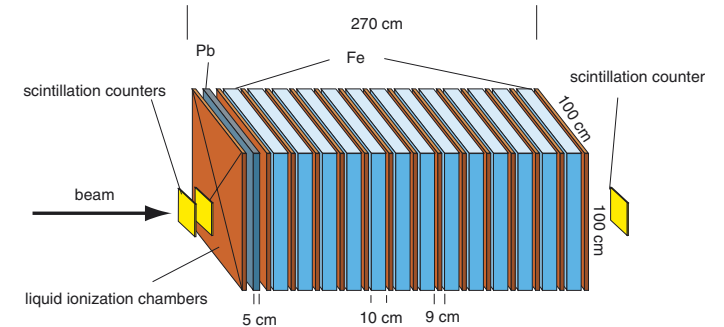
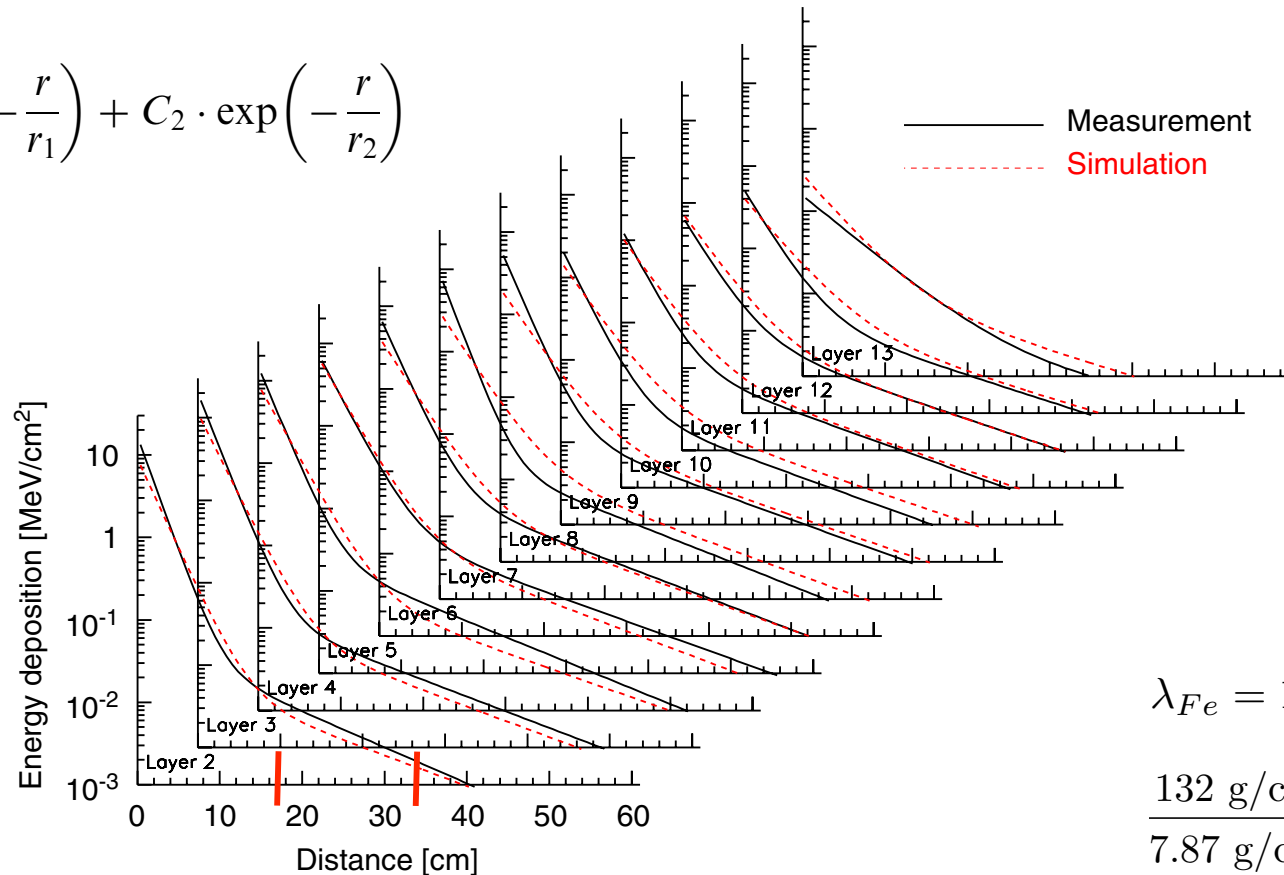


Fig. 2. Schematic view of the sampling calorimeter.

S. Plewnia et al. / Nuclear Instruments and Methods in Physics Research A 566 (2006) 422–432

427

$$\delta E(r) = C_1 \cdot \exp\left(-\frac{r}{r_1}\right) + C_2 \cdot \exp\left(-\frac{r}{r_2}\right)$$



$$\lambda_{Fe} = 132 \text{ g/cm}^2$$

$$\frac{132 \text{ g/cm}^2}{7.87 \text{ g/cm}^3} \approx 16.8 \text{ cm}$$

Fig. 9. Lateral distribution of the energy deposition in different layers of the calorimeter for 300 GeV hadrons. Measurements (solid lines) and simulations (dashed lines) are represented by parameterizations according to Eq. (5).

Energy measurement - calorimeter

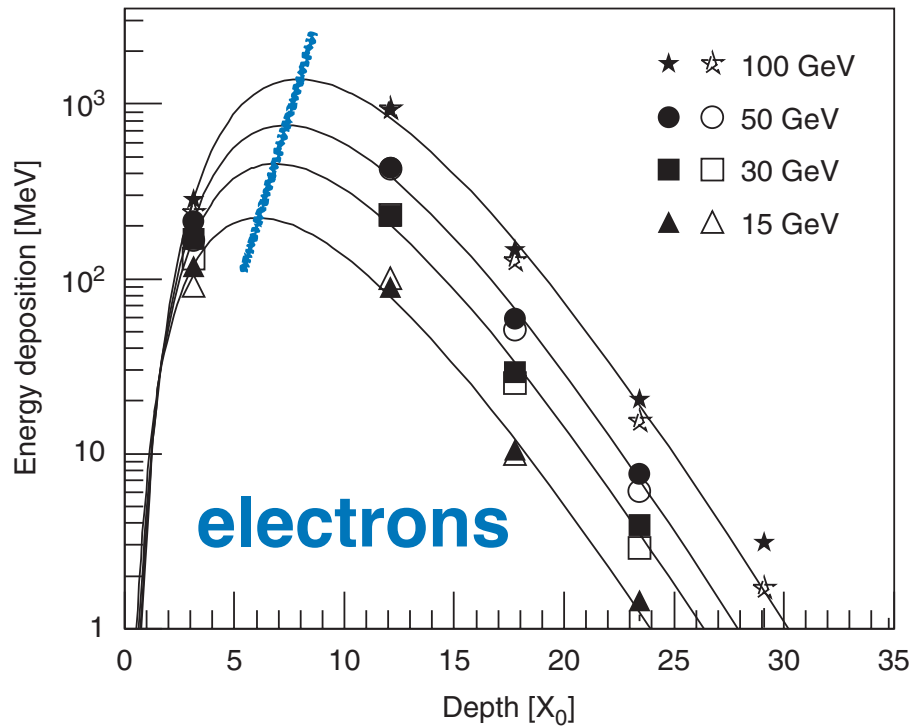


Fig. 16. Energy deposition as function of depth in the calorimeter for electrons. Shown are measurements (filled symbols) and results of simulations (open symbols). The lines represent fits to the measurements according to Eq. (7).

The data points have been fitted using the approach

$$E_{\text{dep}}(t) = A \cdot t^B \cdot \exp(-t/C) \quad (7)$$

originally introduced for electromagnetic cascades [28]. The absorber depth t is measured in interaction lengths λ_i or radiation lengths X_0 for hadrons and electrons, respectively. B characterizes the growth of the cascade before the maximum and C the exponential decrease at large depths.

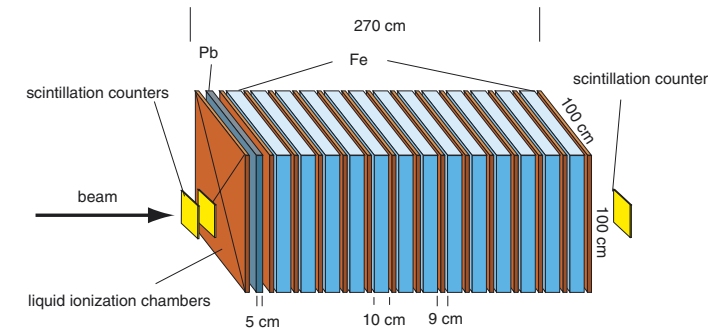


Fig. 2. Schematic view of the sampling calorimeter.

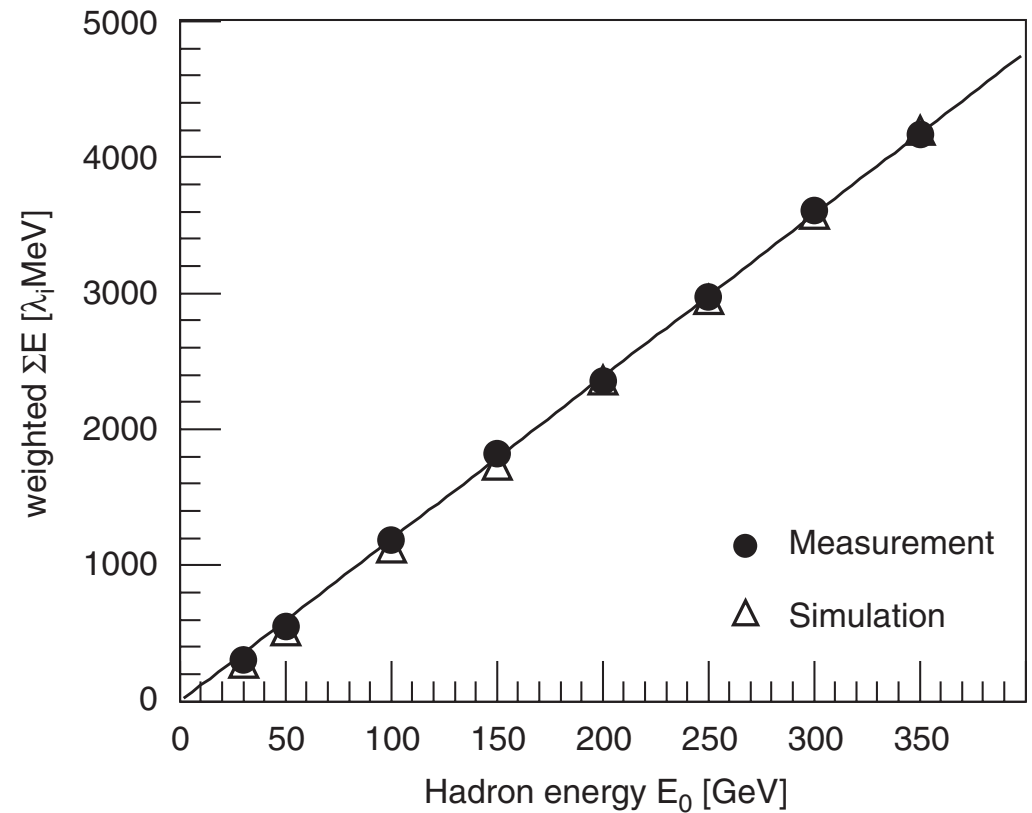


Fig. 17. Energy sum in the calorimeter as function of the incident hadron energy. The energy in each layer is weighted with the amount of absorber in front of the layer.

The number of low-energy ($1 - 10 \text{ GeV}$) muons increases as the shower develops then reaches a plateau because muons rarely interact. The attenuation of the muon component due to muon decay and energy loss is relatively slow. In contrast, the number of electrons and positrons declines rapidly after maximum because radiation and pair production subdivides the energy down to the critical energy ($E_c \sim 80 \text{ MeV}$ – see 5.3) after which electrons lose their remaining energy to ionization quickly. These basic features of longitudinal development of showers are illustrated in the right panel of Figure 16.1.

The left panel of Figure 16.1 shows the lateral distributions of the different components. Secondary hadrons are produced at a typical, almost energy-independent transverse momentum of $p_\perp \sim 350 - 400 \text{ MeV}$, leading to a large angle of low-energy hadrons relative to the shower axis. In contrast, most of the EM particles are in the cascades initiated by high-energy π^0 nearly parallel to the hadronic core. Their lateral spread comes mainly from multiple Coulomb scattering.¹ Thus the lateral distribution of muons is wider than that of EM particles because they are mainly produced in the decay of low-energy pions [505, 506]. For the same reason, hadronic interactions at low energy ($E \lesssim 200 \text{ GeV}$) largely determine the total muon yield [507, 508]. In round numbers the muons make up of order $\sim 10\%$ of the charged particles. In the EM component, the γ -rays outnumber the e^\pm by a factor of ~ 10 .

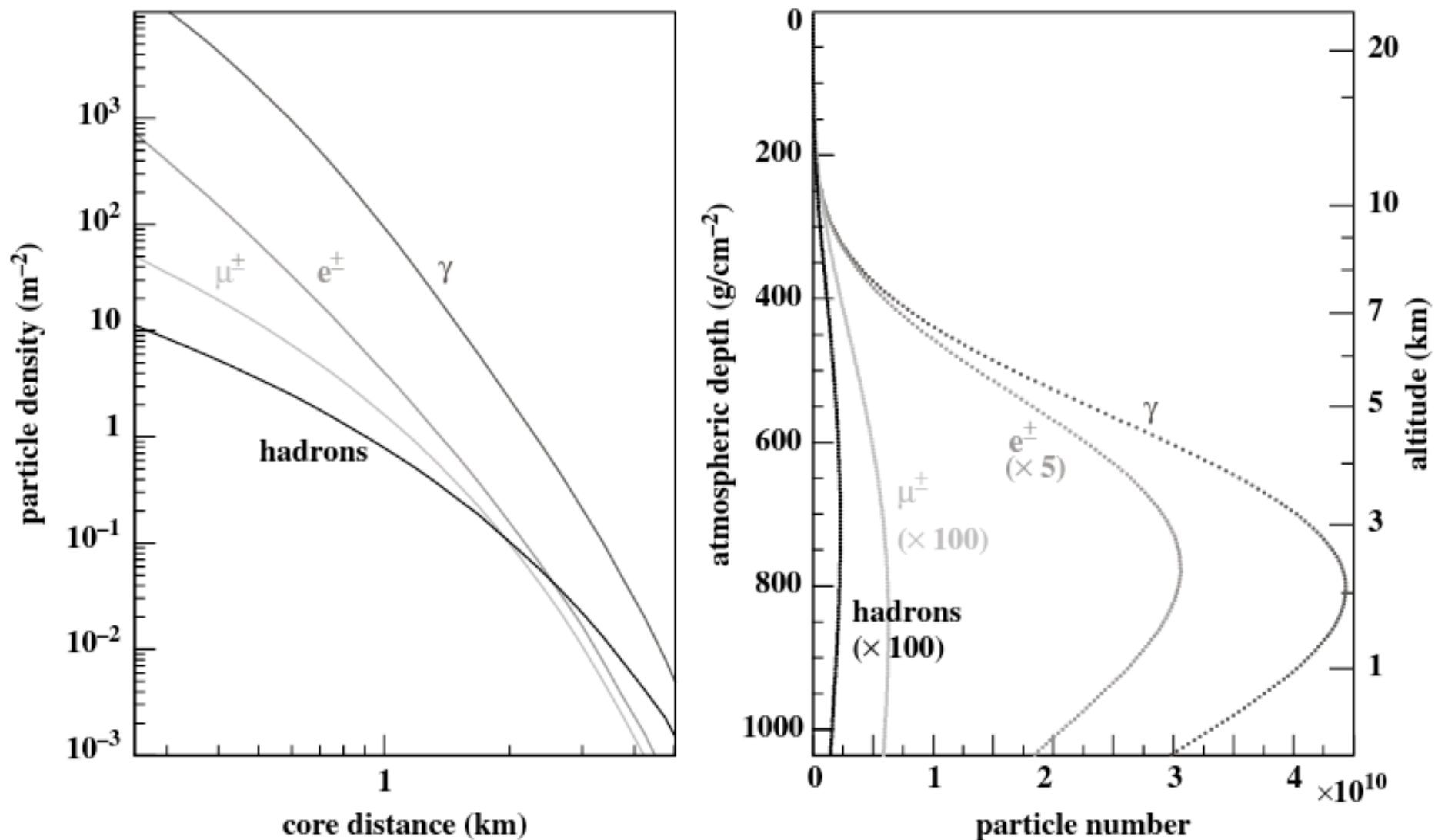
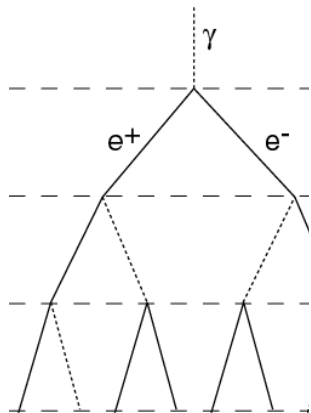


Figure 16.1 Average lateral and longitudinal shower profiles for vertical, proton-induced showers at 10^{19} eV. The lateral distribution of the particles at ground is calculated for 870 g/cm^2 , the depth of the Auger Observatory. The energy thresholds of the simulation were 0.25 MeV for γ , e^\pm and 0.1 GeV for muons and hadrons (from [33]).

A Matthews Heitler Model – Electromagnetic Cascades



pair production $\gamma \rightarrow e^+e^-$

bremsstrahlung $e \rightarrow e+\gamma$

splitting length $d=X_0 \ln 2$

radiation length $X_0=36.7 \text{ g/cm}^2$



Available online at www.sciencedirect.com

SCIENCE @ DIRECT®

Astroparticle Physics 22 (2005) 387–397

Astroparticle
Physics

www.elsevier.com/locate/astropart

A Heitler model of extensive air showers

J. Matthews *

Department of Physics and Astronomy, Louisiana State University, Baton Rouge, LA 70803, USA
Department of Physics, Southern University, Baton Rouge, LA 70813, USA

Received 8 August 2004; received in revised form 3 September 2004; accepted 13 September 2004
Available online 26 October 2004

after n splitting lengths: $x = nX_0 \ln 2$ and $N = 2^n = \exp\left(\frac{x}{X_0}\right)$

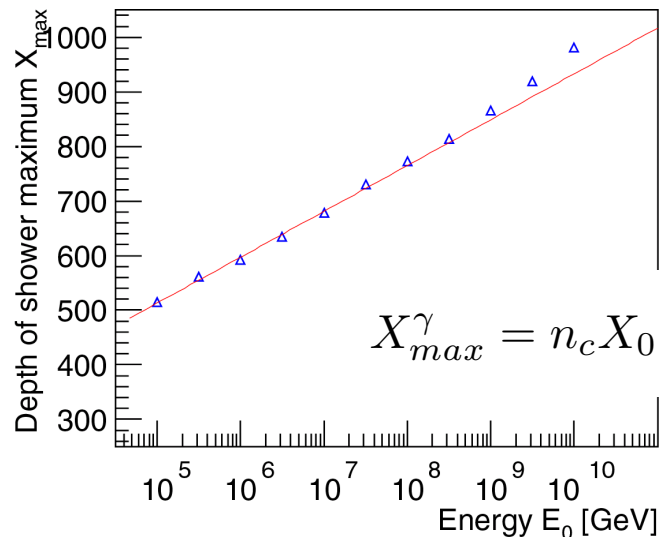
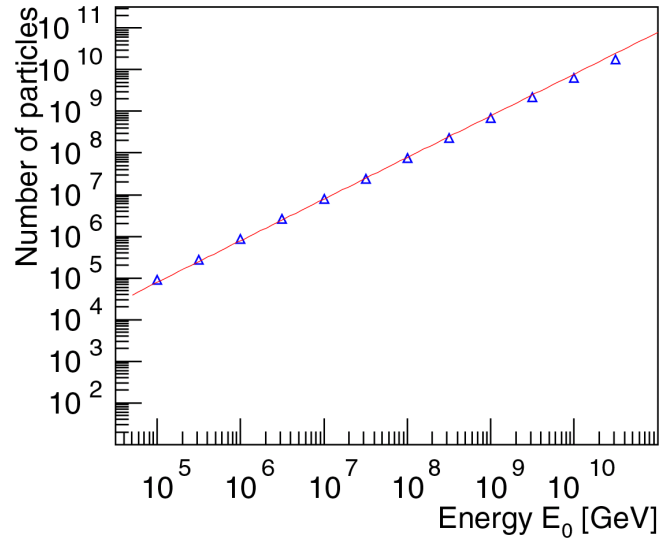
energy per particle $E = E_0/N$ critical energy $E_c^e = 85 \text{ MeV}$

number of particles at shower maximum

$$N_{max} = 2^{n_c} = \frac{E_0}{E_c^e} \quad n_c = \frac{\ln\left(\frac{E_0}{E_c^e}\right)}{\ln 2}$$

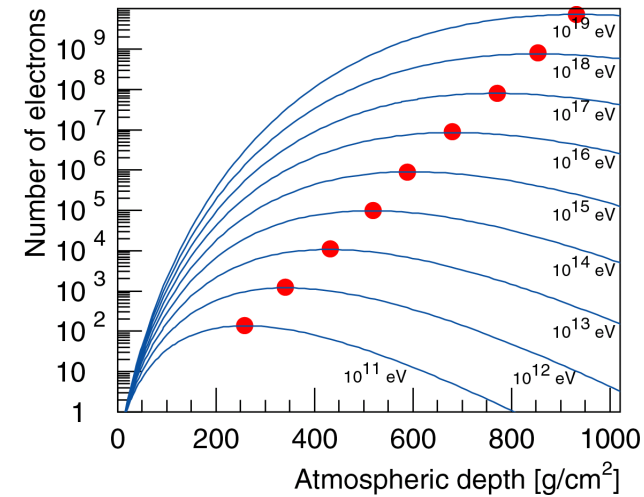
A Matthews Heitler Model – Electromagnetic Cascades

J. Matthews, Astrop. Phys. 22 (2005) 387



number of electrons at shower maximum

$$N_e^{max} = \frac{E_0}{gE_c^e} \approx 9.0 \cdot 10^5 \frac{E_0}{\text{PeV}} \quad g \approx 13$$

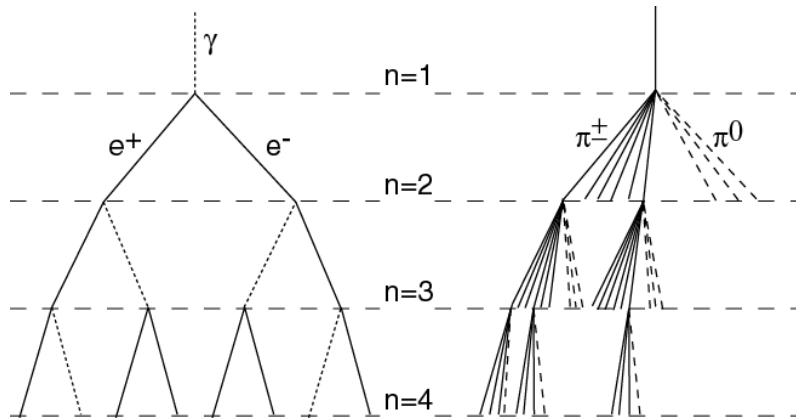


depth of shower maximum



$$X_{max}^\gamma = n_c X_0 \ln 2 = X_0 \ln \left(\frac{E_0}{E_c^e} \right) \approx 597 \frac{\text{g}}{\text{cm}^2} + 84 \frac{\text{g}}{\text{cm}^2} \lg \left(\frac{E_0}{\text{PeV}} \right)$$

A Matthews Heitler Model – Hadronic Cascades



hadronic interaction $\pi+A \rightarrow \pi^0 + \pi^+ + \pi^-$

interaction length $\lambda_{\pi\text{-air}} \sim 120 \text{ g/cm}^2$

$\pi \rightarrow$ hadronic interaction
 \rightarrow decay

„critical energy“ $E_c^\pi \sim 20 \text{ GeV}$

in each interaction $\frac{3}{2}N_{ch}$ particles: $N_{ch} \pi^{+-}$ and $\frac{1}{2} N_{ch} \pi^0$ $N_{ch} \sim 10$

after n interactions $N_\pi = (N_{ch})^n$ $E_\pi = \frac{E_0}{\left(\frac{3}{2}N_{ch}\right)^n}$

after n_c interactions $E_\pi = E_c^\pi$: $n_c = \frac{\ln E_0 / E_c^\pi}{\ln \frac{3}{2} N_{ch}} = 0.85 \lg \left(\frac{E_0}{E_c^\pi} \right)$

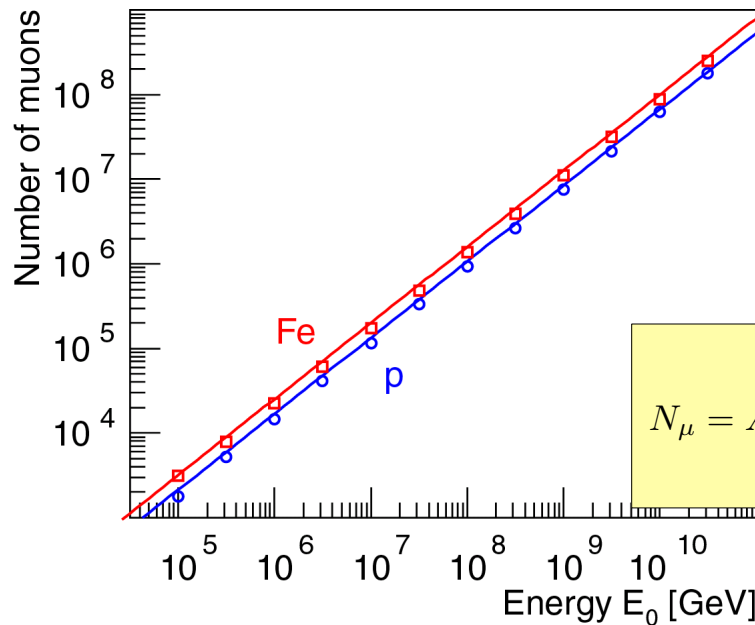
superposition model

particle $(E_0, A) \rightarrow A$ proton showers with energy E_0/A

JRH, Mod. Phys. Lett. A 22 (2007) 1533

A Matthews Heitler Model – N_μ and N_e

Number of muons at shower maximum



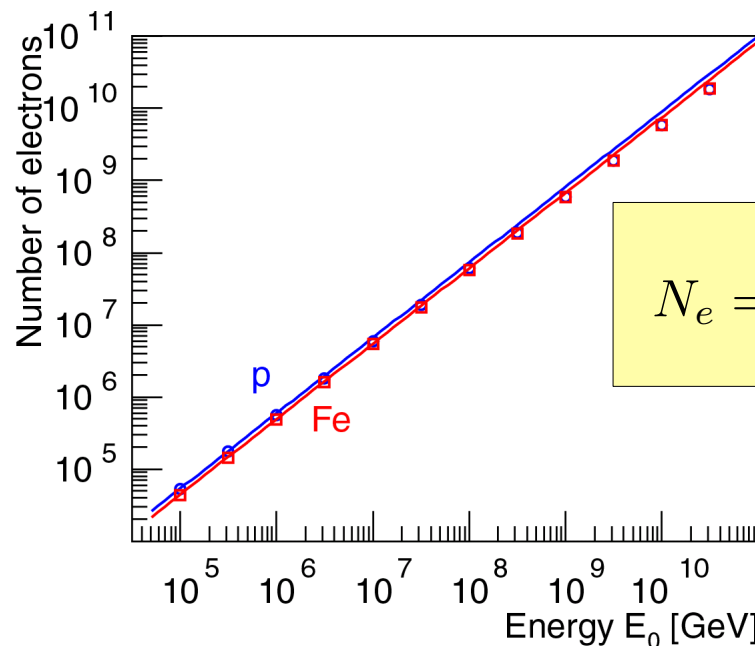
$$N_\mu = N_\pi = (N_{ch})^{n_c}$$

$$\ln N_\mu = n_c \ln N_{ch} = \beta \ln \left(\frac{E_0}{E_c^\pi} \right)$$

$$N_\mu = A \left(\frac{E_0}{AE_c^\pi} \right)^\beta = \left(\frac{E_0}{E_c^\pi} \right)^\beta A^{1-\beta} \approx 1.7 \cdot 10^4 \cdot A^{0.10} \left(\frac{E_0}{1 \text{ PeV}} \right)^{0.90}$$

J. Matthews, Astrop. Phys. 22 (2005) 387

Number of electrons at shower maximum



$$\frac{E_{em}}{E_0} = \frac{E_0 - N_\mu E_c^\pi}{E_0} = 1 - \left(\frac{E_0}{AE_c^\pi} \right)^{\beta-1}$$

$$N_e = \frac{E_{em}}{gE_c^e} \approx 6 \cdot 10^5 \cdot A^{-0.046} \left(\frac{E_0}{1 \text{ PeV}} \right)^{1.046}$$

JRH, Mod. Phys. Lett. A 22 (2007) 1533

A Matthews Heitler Model – N_μ vs. N_e

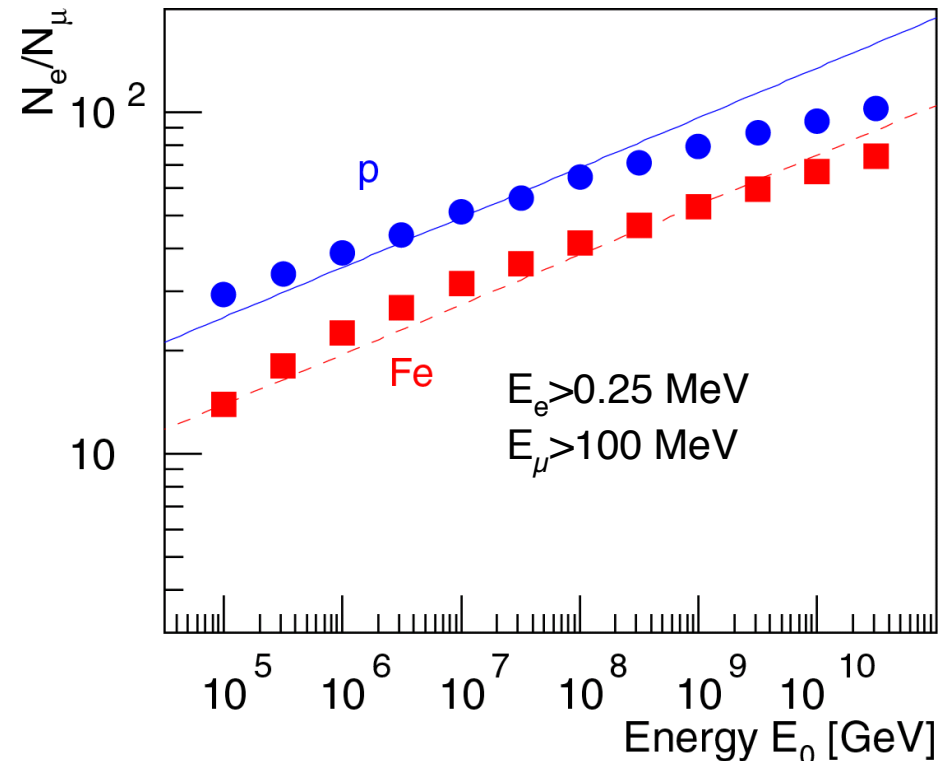
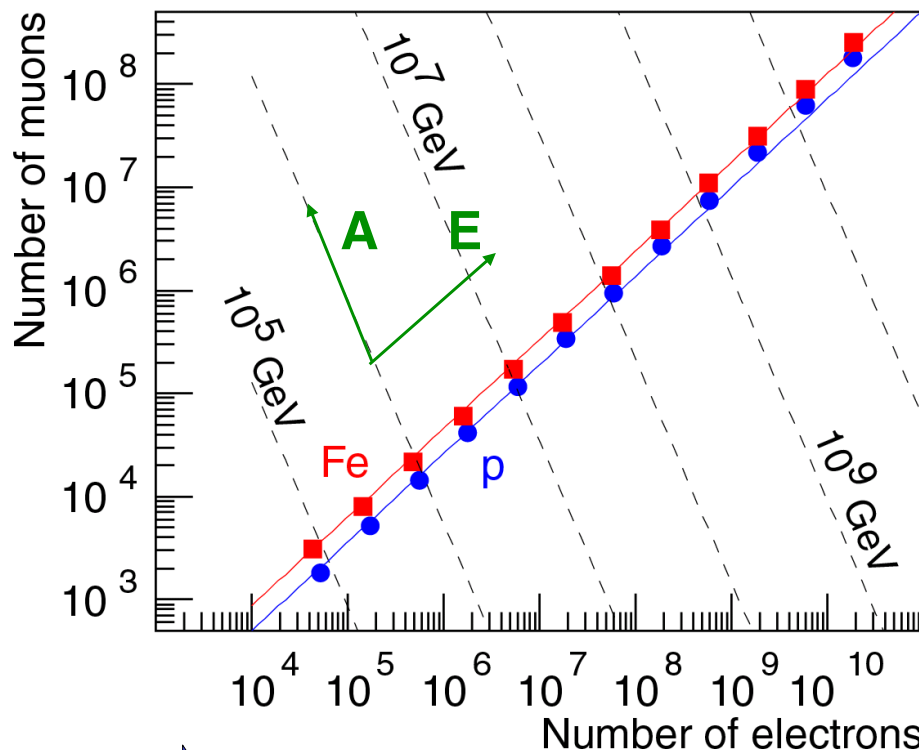
N_e - N_μ plane

$$N_\mu|_{A=const} \approx 0.18 A^{0.14} N_e^{0.86}$$

$$N_\mu|_{E_0=const} \approx 5.77 \cdot 10^{16} \left(\frac{E_0}{1 \text{ PeV}} \right) N_e^{-2.17}$$

N_e - N_μ ratio

$$\frac{N_e}{N_\mu} \approx 35.1 \cdot \left(\frac{E_0}{A \cdot 1 \text{ PeV}} \right)^{0.15}$$



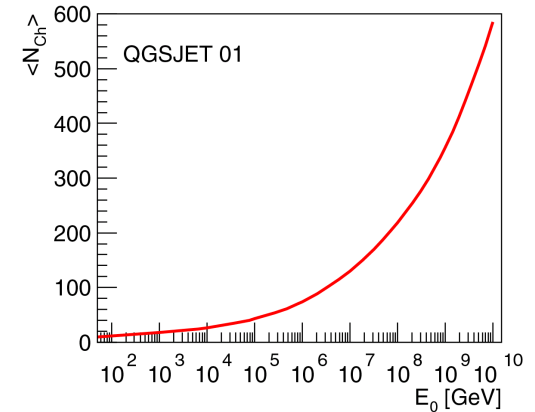
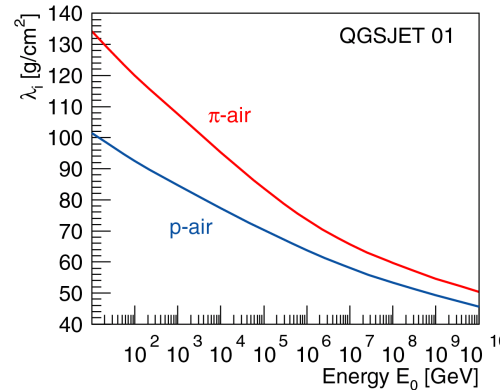
➔ estimator for mass A of primary particle

A Heitler Model – X_{max}

$$X_{max}^p = \lambda_i^{p-air} \ln 2 + X_0 \ln \left(\frac{\kappa E_0}{3N_{ch} E_c^e} \right)$$

proton air interaction length

$$\lambda_i^{p-air} = \xi + \zeta \lg \frac{E_0}{\text{PeV}} \quad \zeta = -4.88 \text{ g/cm}^2$$



multiplicity of charged particles produced in π -N interactions

$$N_{ch} = N_0 \left(\frac{E_0}{\text{PeV}} \right)^\eta \quad \eta = 0.13$$

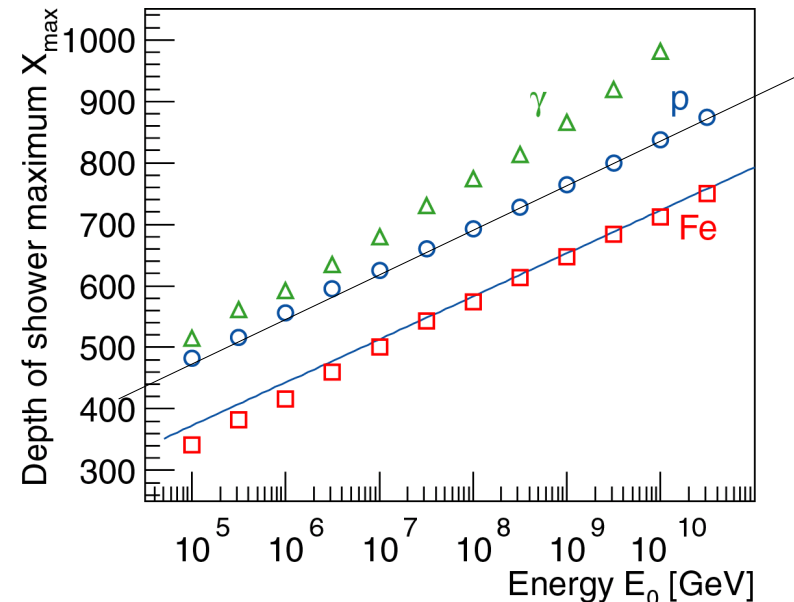
$$X_{max}^p = \xi \ln 2 - X_0 \left(\frac{3N_0 E_c^e}{\kappa \cdot \text{PeV}} \right) + \Lambda^p \lg \left(\frac{E_0}{\text{PeV}} \right)$$

elongation rate

e/m shower $\Lambda^\gamma = X_0 \ln 10 \approx 84.4 \text{ g/cm}^2$

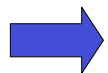
proton shower

$$\Lambda^p = X_0 \ln 10 - \eta X_0 \ln 10 + \zeta \ln 2 \approx 70 \text{ g/cm}^2$$



X_{max} for heavy nuclei

$$X_{max}^A = X_{max}^p - X_0 \ln A$$



estimator for mass A of primary particle

JRH, Mod. Phys. Lett. A 22 (2007) 1533

A Matthews Heitler Model – mass resolution in EAS measurements

depth of shower maximum

$$X_{\max}^A = X_{\max}^p - X_0 \ln A$$

radiation length $X_0=36.7 \text{ g/cm}^2$

typical uncertainty

$$\Delta X_{\max} \approx 20 \text{ g/cm}^2$$


expected mass resolution

 $\Delta \ln A \approx 0.8 - 1$

electron-muon ratio

$$\lg(N_e/N_\mu) = C - 0.065 \ln A.$$

$$\Delta \frac{N_e}{N_\mu} \approx 16\% - 20\%$$

 **4 to 5 mass groups
p, He, CNO, (Si), Fe**

16.3 Muons in air showers

Solution of the cascade equation 5.1 for EM particles was discussed in the previous chapter. Solving for single hadronic cascades is also possible by a combination of numerical integration and analytical expressions (see e.g. [511–514]). However the complexity of hadronic multiparticle production and the need to treat particle decays does not allow the derivation of compact analytic expressions for hadronic showers. With increasing computing power at hand it has become the standard to calculate hadronic showers numerically and to parametrize the results if needed. We will refer to the cascade equation framework in this chapter to illustrate some features of showers, while referring to results of full simulations as needed.

One-dimensional hybrid approach to extensive air shower simulation

2.2. Hadronic cascade equations

The backbone of a hadron-initiated extensive air shower is the hadronic cascade which develops via particle propagation, decay, and interaction with air nuclei of both the initial particle and of produced secondary hadrons. The corresponding integro-differential equations are given by [7] (see also [13])

$$\begin{aligned}
 \frac{\partial h_a(E, X)|_T}{\partial X} = & - \frac{h_a(E, X)|_T}{\lambda_a(E)} - h_a(E, X)|_T \frac{\left| \frac{dL}{dX} \right|_T}{\tau_a(E)c} \\
 & + \frac{\partial}{\partial E} (\beta_a^{\text{ion}}(E) h_a(E, X)|_T) \\
 & + \sum_d \int_E^{E_{\text{max}}} dE' h_d(E', X)|_T \left[\frac{W_{d \rightarrow a}(E', E)}{\lambda_d(E')} \right. \\
 & \left. + D_{d \rightarrow a}(E', E) \frac{\left| \frac{dL}{dX} \right|_T}{\tau_d(E')c} \right] + S_a^{\text{had}}(E, X)|_T, \quad (1)
 \end{aligned}$$

where $h_a(E, X)|_T$ are the differential energy spectra of hadrons of type a with energy E at depth position X along a given straight line trajectory T (in the following the T -symbol will be omitted), $\beta_a^{\text{ion}}(E) = -dE_a/dX$ is the ionization energy loss of particle a per depth unit. A muon is treated like a hadron, but without interaction term.

The first term in the r.h.s. of Eq. (1) represents the decrease of hadron number due to interactions with air nuclei

$$\frac{dh_a}{dX} = - \frac{h_a}{\lambda_a}, \quad (2)$$

with the corresponding mean free path $\lambda_a = m_{\text{air}}/\sigma_{\text{inel}}^{a\text{-air}}$, where m_{air} is the average mass of air molecules and $\sigma_{\text{inel}}^{a\text{-air}}$ is the hadron a -air nucleus inelastic cross section.

The second term describes particle decay, with the decay rate on a path dL being

$$dh_a = -h_a \frac{dL}{\tau_a c}, \quad (3)$$

where τ_a is the life time of hadron a in the lab. system, related to the proper life time $\tau_a^{(0)}$ by $\tau_a = \tau_a^{(0)} E/m_a$, with m_a being the hadron mass and c the velocity of light. From the definition of slant depth (28) follows

$$\left| \frac{dL}{dX} \right| = \frac{1}{\rho_{\text{air}}(X)}. \quad (4)$$

The third term in Eq. (1) takes into account particle ionization energy losses and the integral term in Eq. (1) represents the production of particles of type a in interactions and decays of higher energy parents of type d , with $W_{d \rightarrow a}(E', E)$, $D_{d \rightarrow a}(E', E)$ being the corresponding inclusive spectra of secondaries.

Finally, the so-called source term $S_a^{\text{had}}(E, X)$ defines the initial conditions and is determined during the MC simulation of above-threshold particle cascading. It consists of contributions of all sub-threshold hadrons produced at that stage

$$S_a^{\text{had}}(E, X) = S_a^{\text{MC} \rightarrow \text{had}}(E, X) = \sum_{i=1}^{N_{\text{source}}^{\text{had}}} \delta_{d_i}^a \delta(E - E_i) \delta(X - X_i) \quad (5)$$

with d_i , E_i , X_i being type, energy, and depth position of the source particles.

One-dimensional hybrid approach to extensive air shower simulation

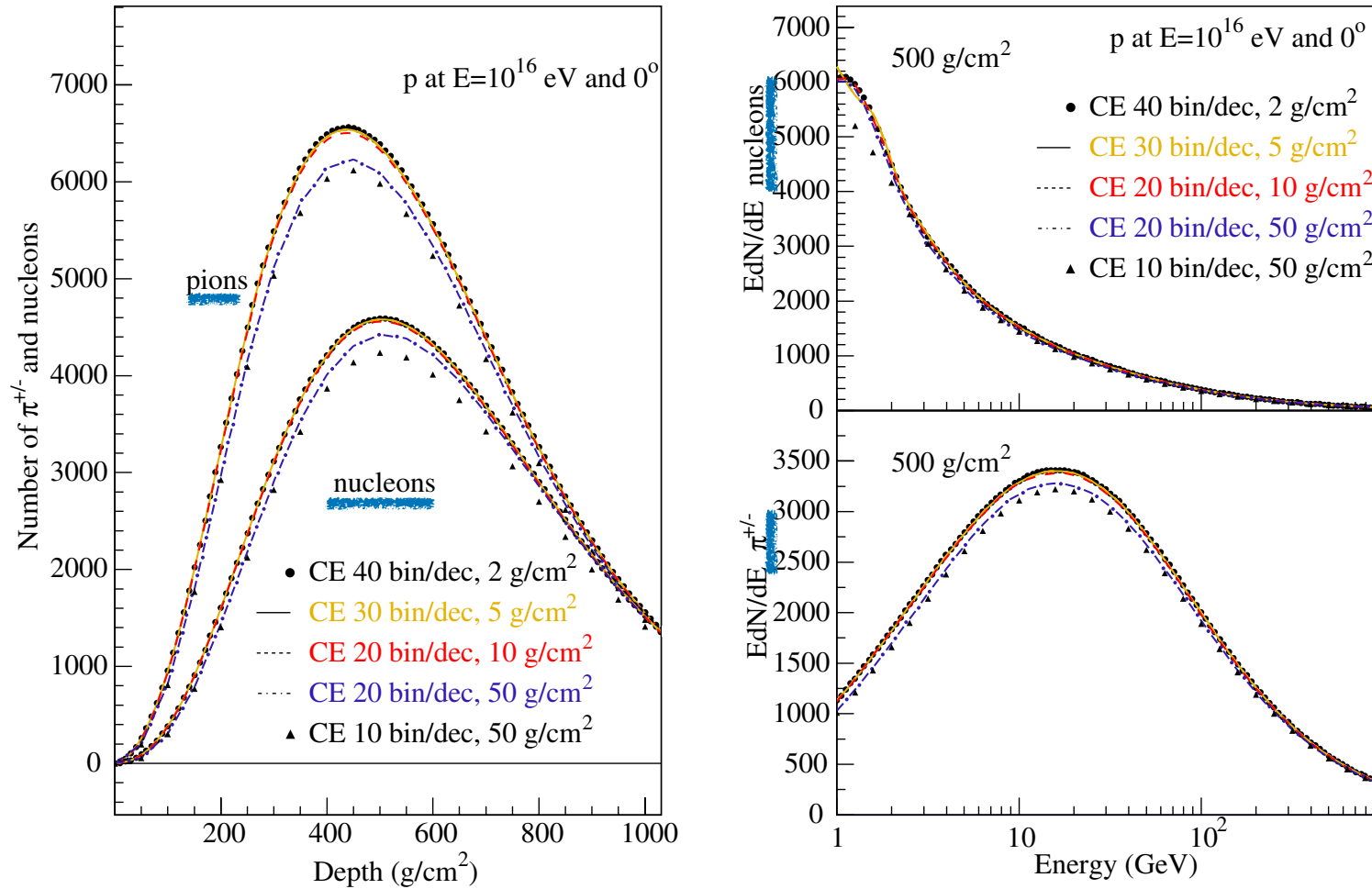


Fig. 1. Average hadronic shower size profiles (left panel) and energy spectra at $X = 500 \text{ g/cm}^2$ (right panel) of nucleons and charged pions for proton-initiated vertical ($\theta = 0^\circ$) showers of 10^{16} eV . Compared are the results of solving numerically the system of cascade equations (CE) with different discretization bin sizes in energy and depth.

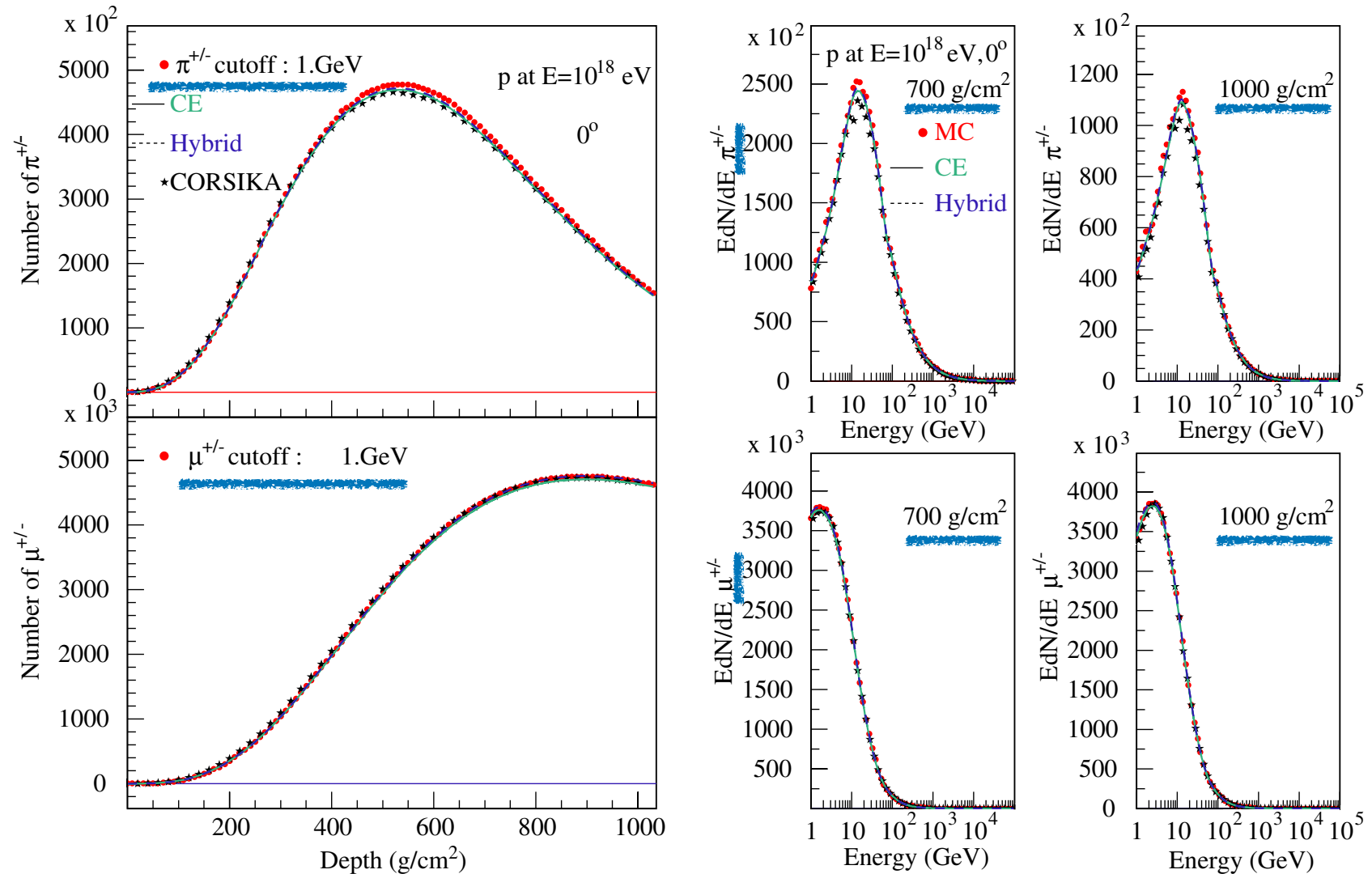


Fig. 2. Average longitudinal shower size profiles (left panel) and energy spectra (right panel) of charged pions and muons with energies above 1 GeV. The calculations were done for proton-initiated vertical showers of 10^{18} eV. Compared are the predictions obtained with CONEX applying the hybrid (dashed line), pure MC (points) and numerical calculation (full line) schemes. In addition CORSIKA predictions are shown as symbols (stars).

One-dimensional hybrid approach to extensive air shower simulation

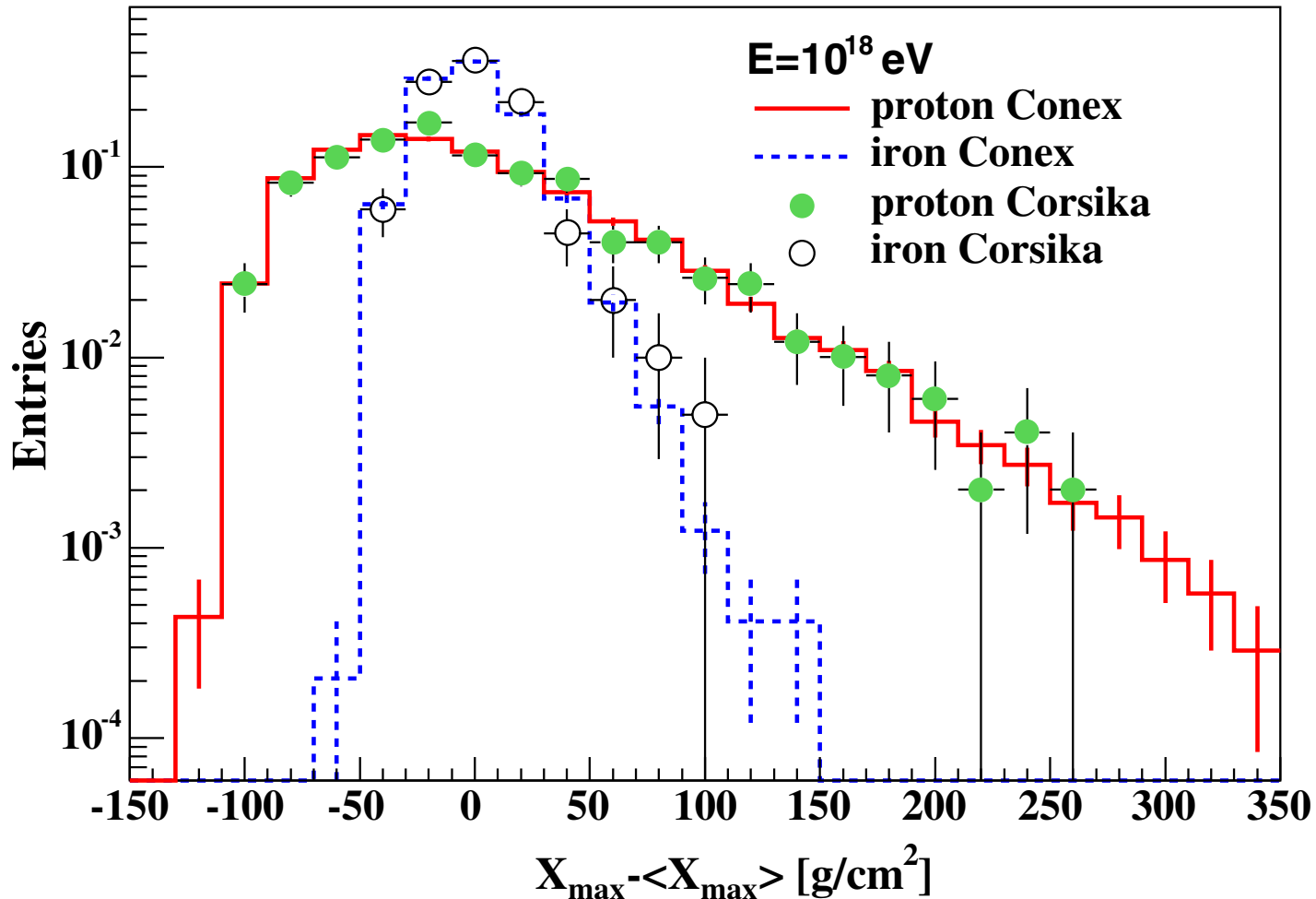


Fig. 7. Fluctuations of the shower maximum depth X_{\max} around corresponding mean shower maximum depths $\langle X_{\max} \rangle$ for a primary energy of 10^{18} eV for proton- and iron-initiated showers simulated with CONEX (lines) and CORSIKA (points).

Because the inclusive production functions (Eq. 5.4) to a good approximation depend only on the ratio of $E_{\text{secondary}}/E_{\text{beam}}$ in the forward fragmentation region, the yield of high-energy, stable secondary hadrons from a single primary proton can also be expected to scale. In other words, we expect the dimensionless combination to satisfy

$$E_i Y(E_i, E_0) = \mathcal{F}_i(\xi_i), \quad \text{with } \xi = \frac{E_i}{E_0}, \quad (16.6)$$

where $Y(E_i, E_0)$ is the differential yield of secondaries of energy E_i from a primary proton of energy E_0 . Here \mathcal{F}_i is integrated over slant depth as compared to Eq. 15.4.

The result of Eq. 16.6 can be used to get the form of the yield of high-energy muons in single air showers. The approximation will apply only for muon energy high enough so that decay of the parent mesons can be neglected in constructing Eq. 16.6. In practice this means TeV and higher ($E_\mu > \epsilon_K / \cos \theta$). From Eq. 5.61, we see that the probability of pion decay at a typical slant depth is proportional to $\epsilon_\pi / (E_\pi \cos \theta)$. (We illustrate here by considering only the contribution due to decay of charged pions. The kaon contribution has the same form.)

The function $F_{ji}(E_i, E_j)$ in Eq. 5.1 is the dimensionless particle yield that follows from the inclusive cross section (integrated over transverse momentum) for a particle of energy E_j to collide with an air nucleus and produce an outgoing particle i with energy $E_i < E_j$. In general, we define

$$F_{ji}(E_i, E_j) \equiv E_i \frac{1}{\sigma_j^{\text{air}}} \frac{d\sigma_{j \text{ air} \rightarrow i}}{dE_i} = E_i \frac{dn_i(E_i, E_j)}{dE_i}, \quad (5.4)$$

where dn_i is the number of particles of type i produced on average in the energy bin dE_i around E_i per collision of an incident particle of type j . All quantities in Eq. 5.4 are defined in the lab system. The relation to center-of-mass quantities can be derived from the definitions in Table 4.1. From Eq. 4.15 it follows that for energetic secondaries, i.e. those with $E_c \gg m_{T,c}$

$$E_c/E_a = x_L \approx x^*. \quad (5.5)$$

(We always define CMS as a projectile on a target *nucleon* even when that nucleon is bound in a nucleus, because nuclear binding energies will usually be much lower than energies of interest in cosmic ray problems we consider.)

muon spectrum from a primary proton of energy E_0 is obtained from convolution of the differential pion yield with the kinematic factor for $\pi^\pm \rightarrow \mu \nu_\mu$:

$$\frac{dN_\mu}{dE_\mu} = \int_{E_\mu}^{E_\mu/r_\pi} \frac{1}{E_\pi (1 - r_\pi)} \frac{\epsilon_\pi}{E_\pi \cos \theta} Y(E_\pi, E_0) dE_\pi, \quad (16.7)$$

where the kinematic limits are as in Eq. 6.18. Rewriting the equation in terms of the scaling variables $\xi_\pi = E_\pi/E_0$ and $\xi_\mu = E_\mu/E_0$, we get

$$\frac{dN_\mu}{d\xi_\mu} = \frac{\epsilon_\pi}{E_\mu \cos \theta} \xi_\mu F(\xi_\mu), \quad (16.8)$$

where

$$F(\xi_\mu) = \int_{\xi_\mu}^{\xi_\mu/r_\pi} \frac{\mathcal{F}(\xi_\pi)}{1 - r_\pi} \frac{d\xi_\pi}{\xi_\pi^3}.$$

Typically, we want the number of muons above an energy sufficient to reach a deep underground detector. The integral of Eq. 16.8 leads to

$$N_\mu(> E_\mu) = \frac{\epsilon_\pi}{E_\mu \cos \theta} \int_{\xi_\mu}^1 z F(z) dz = \frac{\epsilon_\pi}{E_\mu \cos \theta} G(\xi_\mu). \quad (16.9)$$

The same argument that leads to the scaling form for the yield of high-energy hadrons in a shower leads to a scaling approximation for the number of hadronic interactions in the shower. Such an approximation is

$$\frac{dn_{\text{int}}}{dz} \sim \delta(1-z) + \frac{1}{z} + 0.77 \frac{(1-z)^3}{z^{1.78}}, \quad (16.10)$$

where $z = E/E_0$ is the energy of the interaction scaled to the primary energy. The first two terms represent interactions of nucleons, the δ -function for the initial interaction and the $1/z$ term for subsequent interactions of nucleons assuming a flat distribution in fractional momentum for the reaction $N + \text{air} \rightarrow N + X$. The last term is due to interactions of mesons.

A check on energy conservation is useful to verify that formula 16.10, though rudimentary, is at least reasonable. Let $K_\pi^{(\gamma)}$ and $K_N^{(\gamma)}$ represent the fraction of the interaction energy that goes into the electromagnetic component in collisions respectively of π^\pm and nucleons. Then the total energy dumped into the electromagnetic component in all interactions is

$$\frac{E_{\text{tot}}}{E_0} = \sum_i K_i \int_0^1 z \frac{dn_i}{dz} dz = 2 K_N^{(\gamma)} + 2.41 K_\pi^{(\gamma)}, \quad (16.11)$$

where the sum is over two kinds of interactions, $i = N$ and $i = \pi^\pm$. Roughly, we expect half the energy of nucleon interactions to go into pions, of which approximately 1/3 is in neutral pions, so $K_N^{(\gamma)} \approx 1/6$. For pion-induced interactions the corresponding number should be somewhat less than 1/3. (If all outgoing particles were pions that shared equally in the energy, the number would be exactly 1/3; however, there is a tendency for the fastest produced pion to carry the charge of the pion that initiates the collision.) Energy conservation is satisfied by Eq. 16.11 if $K_N^{(\gamma)} \approx 1/6$ and $K_\pi^{(\gamma)} \approx 0.28$.

Assuming that most of the hadronic interactions are charged pions, the last term in Eq. 16.10 is equivalent to $\mathcal{F}(\xi_\pi) = 0.77(1 - \xi_\pi)^3(\xi_\pi)^{-0.78}$. Substitution of this form into Eqs. 16.8 and 16.9 leads to the result

$$G(\xi_\mu) \propto \left(\frac{E_0}{E_\mu} \right)^{0.78} \quad (16.12)$$

for $\epsilon_\pi \ll E_\mu \ll E_0$. A standard version of Eq. 16.9 that includes a threshold factor is

$$\langle N_\mu(> E_\mu) \rangle \approx A \times \frac{0.0145 \text{ TeV}}{E_\mu \cos \theta} \left(\frac{E_0}{A E_\mu} \right)^{0.757} \left(1 - \frac{A E_\mu}{E_0} \right)^{5.25}. \quad (16.13)$$

Here A is the mass of the parent nucleus, and the superposition approximation has been used, as explained in the next section.

The same starting point (Eq. 16.10) can also be used to obtain an approximation for the bulk of low-energy muons in air showers at the surface. For a simple estimate, assume that all charged pions with $E_\pi < \epsilon_\pi$ decay and all higher-energy charged pions interact. The spectrum of low-energy charged pions produced in the shower is then

$$\frac{dN_\pi}{dE_\pi} \sim \sum_i \int_{\epsilon_\pi}^{E_0} \frac{F_{i\pi^\pm}(x_\pi)}{E_\pi} \frac{dn_i}{dz} \frac{dE}{E_0}, \quad (16.14)$$

where $x_\pi = E_\pi/E$ and $F_{i\pi}$ is the inclusive cross section for $i \rightarrow \pi$ as defined in Eq. 5.4. Changing variables gives

$$\frac{dN_\pi}{dE_\pi} \sim \frac{1}{E_\pi} \sum_i \int_{\epsilon_\pi/E_0}^1 F_{i\pi^\pm}\left(\frac{E_\pi}{zE_0}\right) \frac{dn_i}{dz} dz. \quad (16.15)$$

For $E_\pi < \epsilon_\pi$ the integral can be approximated by evaluating the inclusive cross section at a small value of its argument where it is nearly constant. Furthermore, for $E_0 \gg \epsilon_\pi \approx 115$ GeV, the integral is dominated by its most divergent term, so

$$\frac{dN_\pi}{dE_\pi} \sim \frac{1}{E_\pi} F_{\pi\pi}(0) \left(\frac{E_0}{\epsilon_\pi}\right)^{0.78}, \quad (16.16)$$

For $E_\pi < \epsilon_\pi$ the integral can be approximated by evaluating the inclusive cross section at a small value of its argument where it is nearly constant. Furthermore, for $E_0 \gg \epsilon_\pi \approx 115$ GeV, the integral is dominated by its most divergent term, so

$$\frac{dN_\pi}{dE_\pi} \sim \frac{1}{E_\pi} F_{\pi\pi}(0) \left(\frac{E_0}{\epsilon_\pi} \right)^{0.78}, \quad (16.16)$$

where we have kept only the dominant meson interactions. The estimate for the total number of muons with $E_\mu > 1$ GeV in a nucleon-initiated shower, assuming one muon per pion, is obtained by integrating Eq. 16.16 up to $E_\pi \sim \epsilon_\pi$:

$$N_\mu(> 1 \text{ GeV}) \sim F_{\pi\pi}(0) \ln \epsilon_\pi (\text{GeV}) \left(\frac{E_0}{\epsilon_\pi} \right)^{0.78} \sim 10 \left(\frac{E_0}{\epsilon_\pi} \right)^{0.78}. \quad (16.17)$$

The numerical estimate comes from estimating

$$F_{\pi^\pm\pi^\pm} = E_\pi \frac{dn_\pi}{dE_\pi} = \frac{dn_\pi}{d \ln E_\pi} \sim \frac{dn_\pi}{dy} \sim \frac{dn_\pi}{d\eta} \sim 2.$$

For comparison, the Akeno experiment [519] finds

$$N_\mu(> 1 \text{ GeV}) \approx 11 (E_0/\epsilon_\pi)^{0.83}. \quad (16.18)$$

Test of interaction models up to 40 PeV by studying hadronic cores of EAS

(The KASCADE Collaboration)

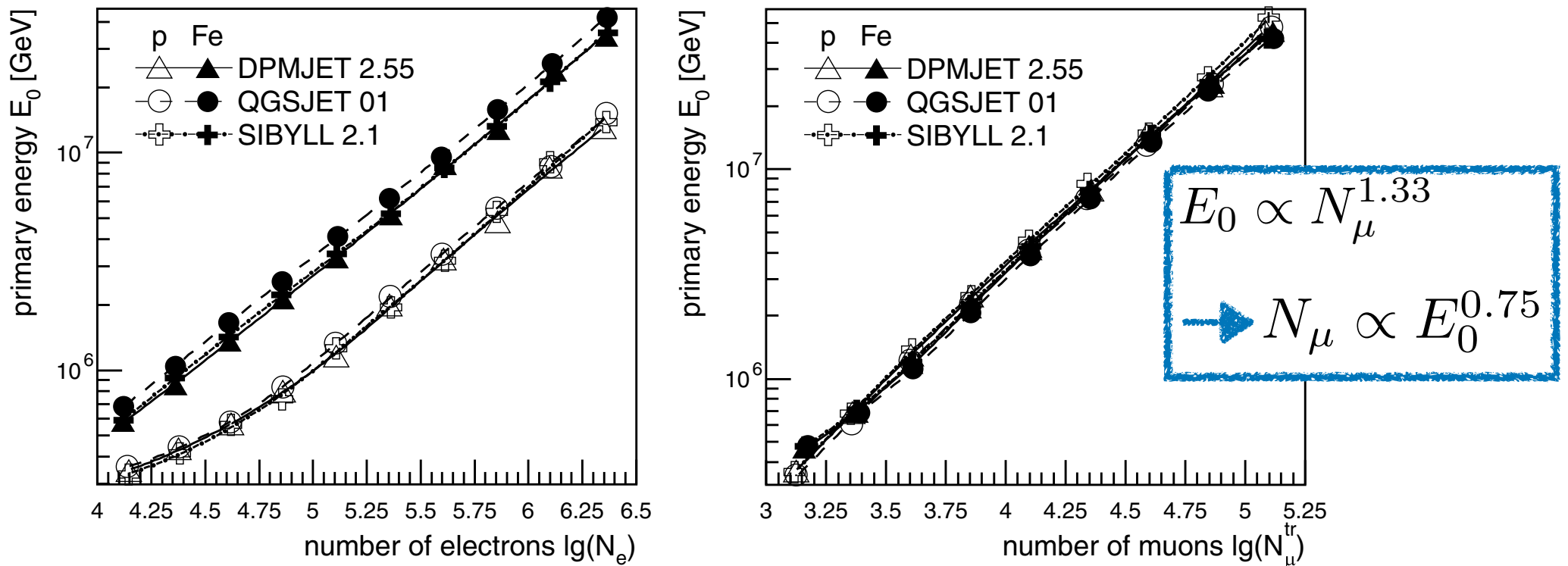
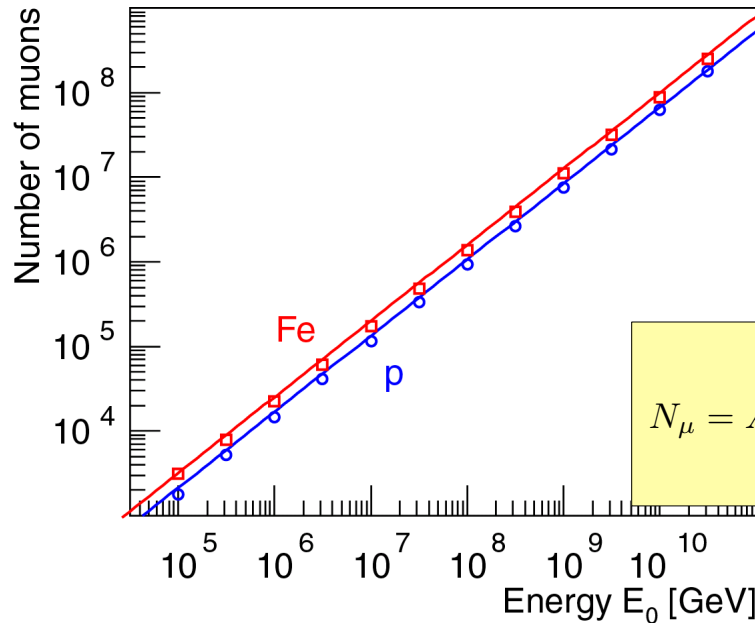


Figure 1. The mean primary energy for the interval of observed electron number N_e (left) and truncated muon numbers N_μ^{tr} (right). Results of simulations for protons and iron nuclei using the indicated high-energy interaction models are shown. The low-energy interactions have been treated by GHEISHA 2002. The lines are five parameter fits to guide the eyes.

A Matthews Heitler Model – N_μ and N_e

Number of muons at shower maximum

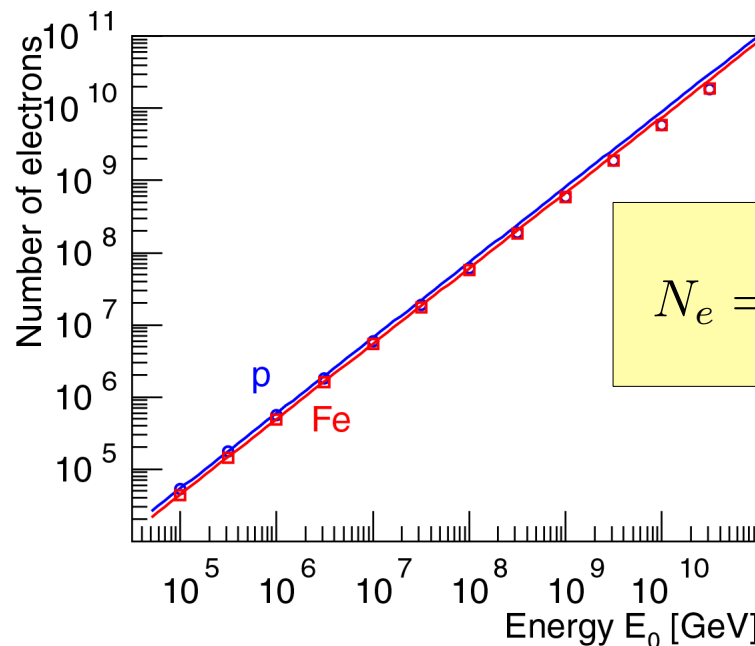


$$N_\mu = N_\pi = (N_{ch})^{n_c}$$

$$\ln N_\mu = n_c \ln N_{ch} = \beta \ln \left(\frac{E_0}{E_c^\pi} \right)$$

$$N_\mu = A \left(\frac{E_0}{AE_c^\pi} \right)^\beta = \left(\frac{E_0}{E_c^\pi} \right)^\beta A^{1-\beta} \approx 1.7 \cdot 10^4 \cdot A^{0.10} \left(\frac{E_0}{1 \text{ PeV}} \right)^{0.90}$$

Number of electrons at shower maximum



$$\frac{E_{em}}{E_0} = \frac{E_0 - N_\mu E_c^\pi}{E_0} = 1 - \left(\frac{E_0}{AE_c^\pi} \right)^{\beta-1}$$

$$N_e = \frac{E_{em}}{gE_c^e} \approx 6 \cdot 10^5 \cdot A^{-0.046} \left(\frac{E_0}{1 \text{ PeV}} \right)^{1.046}$$

16.4 Nuclei and the superposition model

With the binding energy of ~ 5 MeV per nucleon being much smaller than the typical interaction energies, one can consider a nucleus of mass A approximately as A independent nucleons. In this superposition model, a nucleus with mass A and energy E_0 is considered as A independent nucleons with energy $E_h = E_0/A$. This leads to the predictions

$$\begin{aligned} N_{\text{em,max}}^A(E_0) &= A \cdot N_{\text{em,max}}^h(E_h/E_c) \approx N_{\text{em,max}}(E_0) \\ X_{\text{max}}^A(E_0) &= X_{\text{max}}(E_0/A) \\ N_{\mu}^A(E_0) &= A \cdot \left(\frac{E_0/A}{E_{\text{dec}}} \right)^{\alpha} = A^{1-\alpha} \left(\frac{E_0}{E_{\text{dec}}} \right)^{\alpha}. \end{aligned} \quad (16.19)$$

From the first line of this equation, we see that if the fraction of energy transferred to the EM shower component were independent of energy there would be no mass dependence of the number of charged particles at shower maximum. In contrast, from the second and third lines, we expect that the depth of maximum and the number of muons both depend on the mass of the primary particle. (Compare Eqs. 16.3 and 16.5.) The heavier the shower-initiating particle the more muons are expected for a given primary energy and the shallower the depth of maximum. Iron showers contain about 40% more muons than proton showers of the same energy and reach their maximum 80 – 100 g/cm² higher in the atmosphere.

One of the important aspects of the superposition model is the fact that, averaged over many showers, the distribution of nucleon interaction points in the atmosphere coincides with that of more realistic calculations accounting for nucleus interactions and breakup into remnant nuclei [520]. Therefore it is not surprising that the superposition model gives a good description of many features of air showers if inclusive observables are concerned such as the mean depth of shower maximum and the number of muons. However, it is not applicable to observables related to correlations or higher order moments [521, 522].

In the superposition approximation according to Eq. 16.19, the relation between primary energy and number of particles at the position of maximum shower development (X_{\max}) is independent of the mass of the primary nucleus, but the position of X_{\max} depends on primary mass as

$$X_{\max} \propto \lambda \ln[E_0/(A E_c)]. \quad (16.20)$$

This equation is a version of the elongation rate theorem to be discussed in the next section. It has the implication that showers generated by heavy primaries develop more rapidly on average (i.e. higher in the atmosphere) than proton showers of the same total energy. On the other hand, the effect is only logarithmic, so it is clear, given the nature of air shower experiments, that the best one can hope for is to be able to distinguish among groups of nuclei with quite different masses. In practice, even this has proved difficult. Another important distinguishing feature of showers generated by heavy nuclei is that fluctuations in their longitudinal development are smaller than those of light nuclei. This is simply because each nucleus is a beam of many incident nucleons.

In reality what happens when a heavy nucleus enters the atmosphere is that it interacts very quickly (recall, for example, that $\lambda \sim 2.3 \text{ g/cm}^2$ for an iron nucleus). In this first collision, however, only a few of the nucleons in the nucleus interact inelastically with an air nucleus to create secondary pions. Several other nucleons and light nuclear fragments may also be released, and there will generally be one heavy fragment. By studying fragmentation histories of nuclei in photographic emulsion and the multiplicities of secondary particles produced in the various fragmentation events, it is possible to build up a more realistic picture of how nuclei break up in the atmosphere and when their constituent nucleons first interact. The procedure is complicated and very approximate, but it serves to give an indication of the reliability of the superposition model. One complication with the analysis is that a subset of the interactions that correspond with interactions on the light nuclei in the emulsion must be selected since the atmosphere consists almost entirely of light nuclei. Another is that there may be a selection bias for events with higher multiplicity. As a consequence, the estimate of the number of nucleons that interact to produce pions may be somewhat overestimated. Figure 16.3 shows the distribution of points of first interaction for the superposition model as compared to that inferred from the data. The distributions become steeper at higher energy because of the increase with energy of the nucleon cross section.

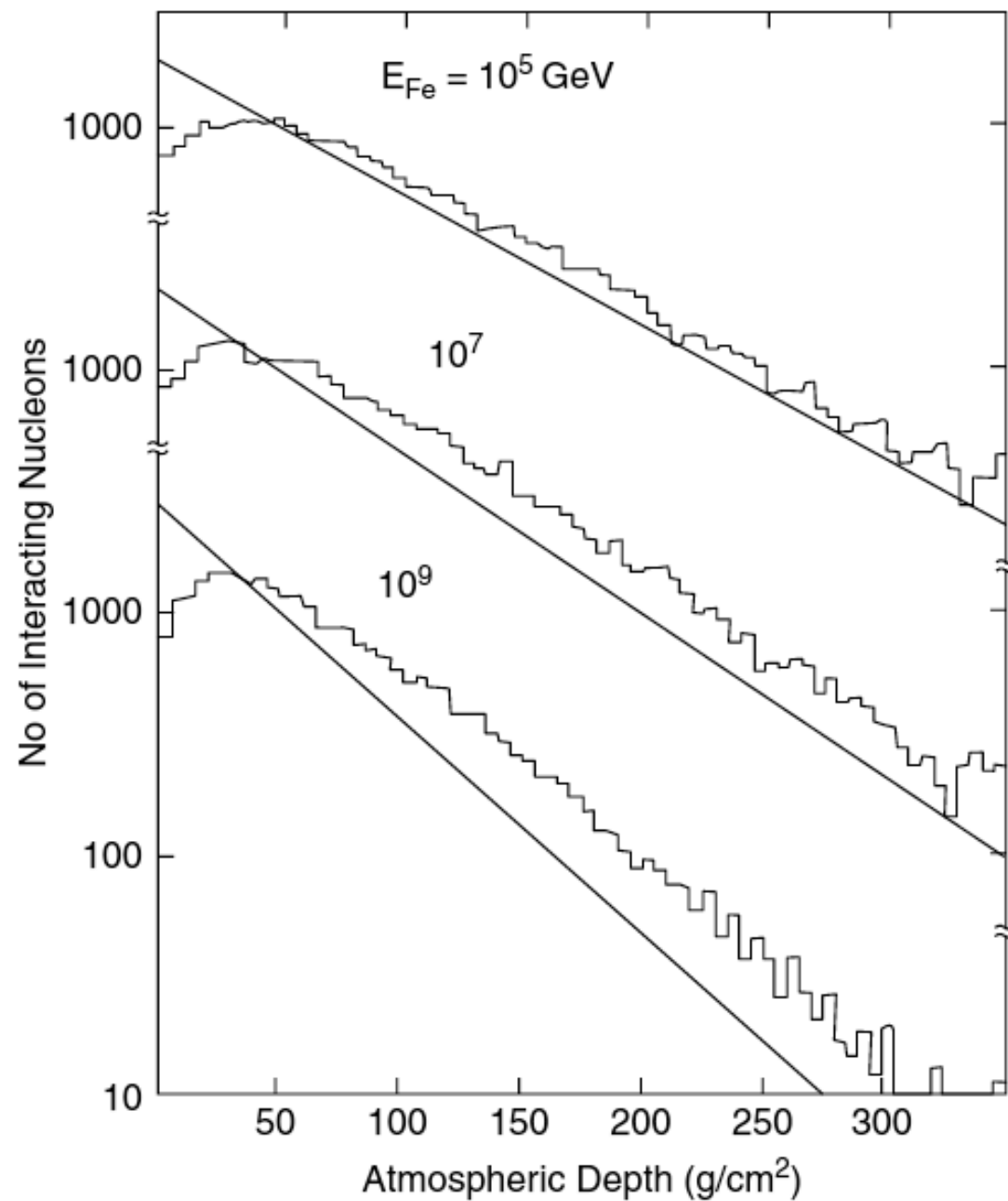


Figure 16.3 Distribution of points of first interaction for nucleons in iron nuclei. Histograms: inferred from data in photographic emulsion. Lines: superposition model. (From Ref. [523])

The general idea of reducing a nucleus-nucleus collision to a series of nucleon-nucleon collisions is called the “wounded nucleon” picture. A simplified version can be constructed directly from the impact parameter representation for the total inelastic cross section from Eq. 4.85. For a proton–nucleus interaction, the total inelastic cross section can be developed as a sum of partial cross sections for exactly N wounded nucleons, see Eqs. 4.83 and 4.85,

where

$$\sigma_N = \int d^2b \frac{[\sigma T(b)]^N}{N!} \exp[-\sigma T(b)],$$

and σ is the nucleon–nucleon cross section. The mean number of wounded nucleons in the target (i.e. the number of nucleon–nucleon collisions) is

$$\langle N \rangle_{pA} = \frac{A \sigma_{pp}}{\sigma_{pA}}.$$

For a nuclear projectile of mass A incident on a target nucleus of mass B the generalization is [524]

$$\langle N \rangle_{AB} = \frac{A \sigma_{pB}}{\sigma_{AB}} + \frac{B \sigma_{pA}}{\sigma_{AB}}.$$

The first term is the number of wounded nucleons in the projectile and the second the number of wounded nucleons in the target. This simple geometrical result predicts that a somewhat larger fraction of the freed nucleons interact to produce pions than the analysis of emulsion data described above.

Considering hadron–nucleus interactions, an approximate and much simpler version of the full Glauber theory is represented by the formula

$$\sigma_{\text{ine}}^{hA} = \int d^2b \{1 - \exp[-\sigma_{\text{tot}}^{hp} T(b)]\}, \quad (4.83)$$

which is the extension of (4.72) to nuclear targets. Here σ_{ine}^{hA} is the inelastic cross section for hadron–nucleus scattering and σ_{tot}^{hp} is the corresponding total hadron–nucleon cross section. The function $T(b)$ is the number density of target nucleons of the nucleus at impact parameter b , folded with the impact parameter profile of the amplitude for hadron–nucleon scattering (see Eq. 4.67)

$$T(b) = \int \rho_N(\vec{r}) A_{hp}(\vec{b} - \vec{b}_N) dz d^2b_N, \quad (4.84)$$

where ρ_N is the number density of nucleons at distance $r = \sqrt{b_N^2 + z^2}$ from the center of the nucleus. The production cross section $\sigma_{\text{prod}}^{hA}$ is given by an expression very similar to (4.83) [175]

$$\sigma_{\text{prod}}^{hA} = \int d^2b \{1 - \exp[-\sigma_{\text{ine}}^{hp} T(b)]\}. \quad (4.85)$$

Two limits follow directly from (4.85). If $\sigma_{\text{ine}}^{hp} T(b)$ is very small then there is no “shadowing”, and

$$\sigma_{\text{prod}}^{hA} \approx \int \sigma_{\text{ine}}^{hp} T(b) d^2b = A \sigma_{\text{ine}}^{hp}. \quad (4.86)$$

In the opposite limit of complete screening ($\sigma_{\text{ine}}^{hp} T(b)$ very large) the integrand of (4.85) is approximately unity out to an effective nuclear radius R_A , so

$$\sigma_{\text{prod}} \approx \pi R_A^2 \propto A^{2/3}. \quad (4.87)$$

In the range of beam momentum 20 – 50 GeV/c, the A -dependence of σ_{ine}^{pA} for $A > 1$ can be approximated by (see [176])

16.5 Elongation rate theorem

The elongation rate describes the change of the depth of the shower maximum per decade in energy [525, 526] and is defined² as

$$D_{10} = \frac{d\langle X_{\max} \rangle}{d \log_{10} E}. \quad (16.21)$$

It is closely related to possible changes of the cosmic ray composition and also depends on the overall characteristics of hadronic interactions at high energy.

From Eq. 15.29 and the fact that the radiation length in air is 37 g/cm^2 , it follows that the elongation rate of electromagnetic showers is $D_{10}^{\text{em}} = \ln(10) \times X_0 \approx 85 \text{ g/cm}^2$ in the energy range in which the LPM effect can be neglected. Assuming that hadronic interactions satisfy Feynman scaling with energy-independent cross sections, the relative energy splitting in the hadronic skeleton of the shower is independent of the primary energy (i.e. it scales with energy). As a consequence, and since the electromagnetic component is dominated by the earliest (i.e. most energetic) generations of hadronic interactions, the elongation rate of the hadronic shower is also D_{10}^{em} in the presence of Feynman scaling.

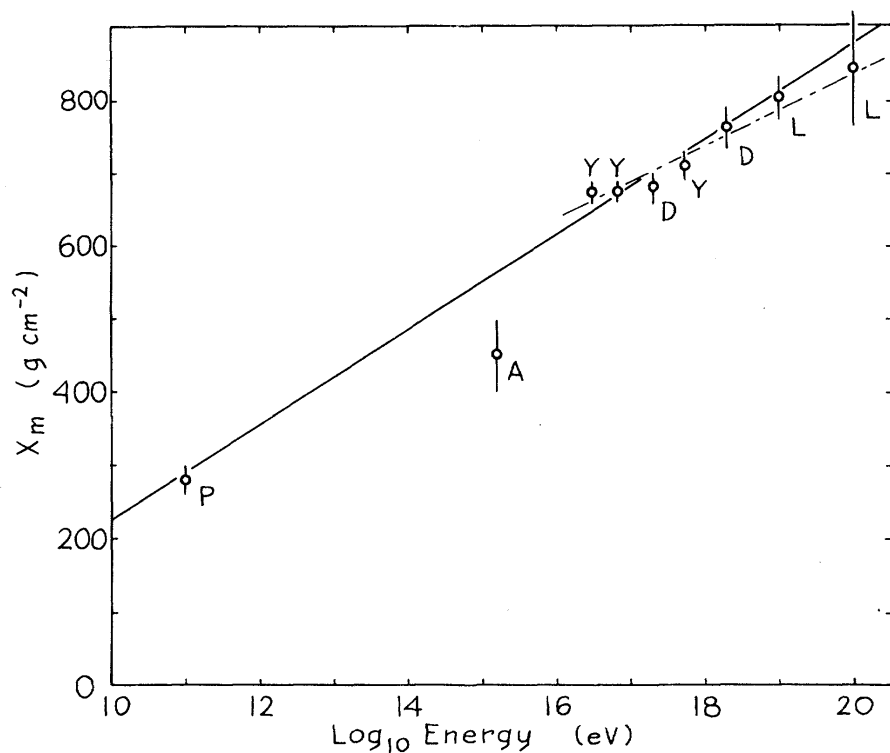
Validity of Scaling to 10^{20} eV and High-Energy Cosmic-Ray Composition

J. Linsley and A. A. Watson^(a)

Department of Physics and Astronomy, University of New Mexico, Albuquerque, New Mexico 87131

(Received 31 July 1980)

It is shown that evidence on cosmic-ray showers of energy 3×10^{16} to 10^{20} eV indicates that scaling in the fragmentation region is valid up to the highest energies if (and only if) hadron-air inelastic cross sections continue to rise in the manner observed at lower energies. It is also shown, with use of additional air-shower evidence, that $\langle \ln A \rangle$, the logarithmic mean primary mass number, changes from (4 ± 2) at 1.6×10^{15} eV to (0 ± 0.6) at and above 3×10^{16} eV.



We discuss the data on X_m in terms of D_e , the so-called “elongation rate,” equal by definition to $dX_m/d \ln E$. X_m is averaged over fluctuations in shower development, and in case of mixed primary composition over the equal-energy mass spectrum. For numerical results we use “ER

FIG. 1. X_m (g cm^{-2}) as a function of energy. The points above 10^{16} eV are identified in Table I. Point *P*, see text and Ref. 14. Point *A*, see text and Ref. 16. Derivation of the solid and dotted lines is described in the text.

The approximation 15.28 is plotted in Figure 15.2 to illustrate how showers evolve over a wide range of primary energy. Shower maximum occurs for $s = 1$. Therefore from Eq. 15.20 with $n = 0$,

$$X_{\max}^{(\text{em})} = X_0 T_{\max} = X_0 \ln \left(\frac{E_0}{E_c} \right) \quad (15.29)$$

and

$$N_{\max}^{(\text{em})} = \frac{0.31}{\sqrt{\ln(E_0/E_c)}} \frac{E_0}{E_c} \sim 10^6 \left(\frac{E_0(\text{GeV})}{10^6} \right). \quad (15.30)$$

Analogous relations for charged particles in hadron-induced showers will be discussed in the following chapter.

Figure 15.2 shows how Eq. 15.28 for electromagnetic cascades evolves over a wide range of primary photon energy. Similar relations among shower age, depth of maximum and size at maximum can be applied in the analysis of showers initiated by primary cosmic rays.

To obtain a more quantitative estimate we consider the depth of maximum of a proton shower which we approximate by that of the EM subshowers produced by the secondaries of the first interaction, see Eq. 16.3,

$$\langle X_{\max}^{\text{had}}(E) \rangle = \langle X_{\max}^{\text{em}}(E/\langle n \rangle) \rangle + \lambda_{\text{int}}, \quad (16.22)$$

where $\langle n \rangle$ is related to the multiplicity of secondaries in the high-energy hadronic interactions in the cascade. From Eq. 16.22 follows

$$\frac{d\langle X_{\max}^{\text{had}}(E) \rangle}{d \log E} = \ln(10) X_0 \left[1 - \frac{d \ln \langle n \rangle}{d \ln E} \right] + \frac{d\lambda_{\text{int}}}{d \log E}, \quad (16.23)$$

which corresponds to the form of the elongation rate theorem given in Ref. [526], namely

$$D_{10}^{\text{had}} \leq \ln(10) X_0 (1 - B_n - B_\lambda), \quad (16.24)$$

with

$$B_n = \frac{d \ln \langle n \rangle}{d \ln E}, \quad B_\lambda = -\frac{\lambda_{\text{int}}}{X_0} \frac{d \ln \lambda_{\text{int}}}{d \ln E}. \quad (16.25)$$

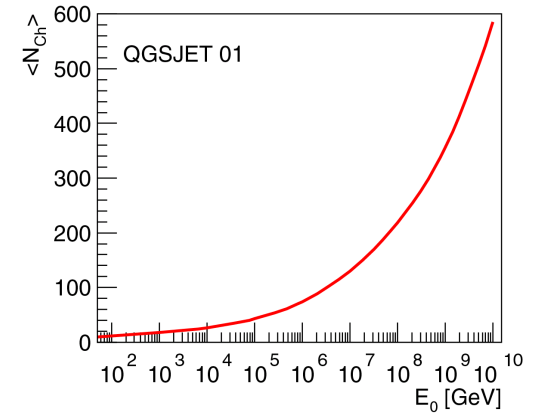
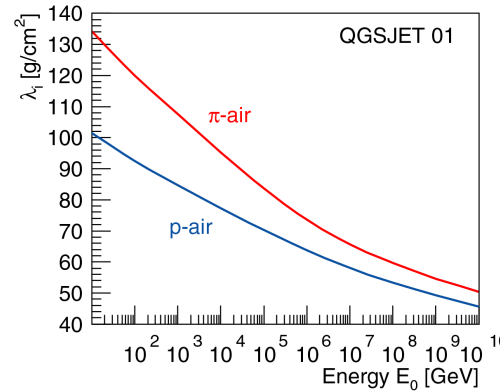
For example, for a multiplicity dependence of $\langle n \rangle \propto E^\delta$ one gets $B_n = \delta$ in the approximation that all secondaries have the same energy.

A Heitler Model – X_{max}

$$X_{max}^p = \lambda_i^{p-air} \ln 2 + X_0 \ln \left(\frac{\kappa E_0}{3N_{ch} E_c^e} \right)$$

proton air interaction length

$$\lambda_i^{p-air} = \xi + \zeta \lg \frac{E_0}{\text{PeV}} \quad \zeta = -4.88 \text{ g/cm}^2$$



multiplicity of charged particles produced in π -N interactions

$$N_{ch} = N_0 \left(\frac{E_0}{\text{PeV}} \right)^\eta \quad \eta = 0.13$$

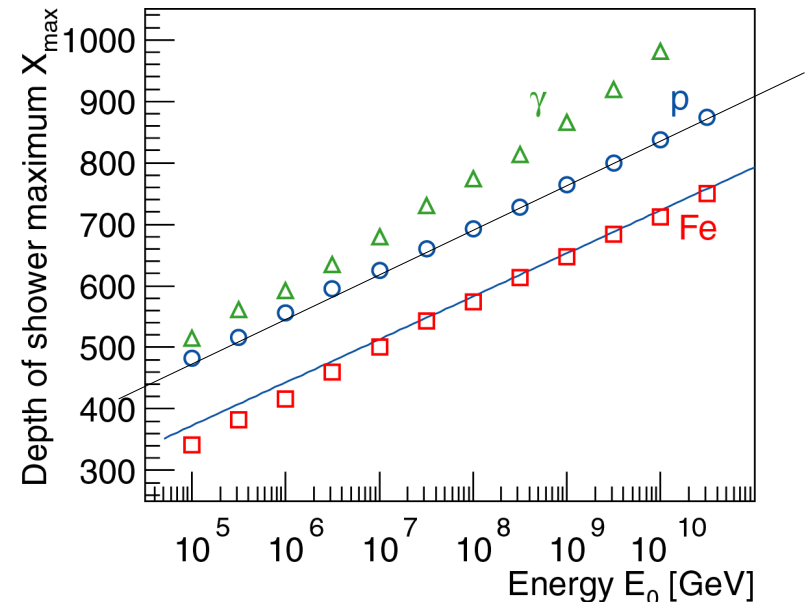
$$X_{max}^p = \xi \ln 2 - X_0 \left(\frac{3N_0 E_c^e}{\kappa \cdot \text{PeV}} \right) + \Lambda^p \lg \left(\frac{E_0}{\text{PeV}} \right)$$

elongation rate

e/m shower $\Lambda^\gamma = X_0 \ln 10 \approx 84.4 \text{ g/cm}^2$

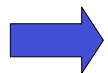
proton shower

$$\Lambda^p = X_0 \ln 10 - \eta X_0 \ln 10 + \zeta \ln 2 \approx 70 \text{ g/cm}^2$$



X_{max} for heavy nuclei

$$X_{max}^A = X_{max}^p - X_0 \ln A$$



estimator for mass A of primary particle

JRH, Mod. Phys. Lett. A 22 (2007) 1533

Averaging over showers with an energy-independent mass composition of primary particles does not change this result as we have from the superposition model

$X_{\max} \propto D_{10}^{\text{had}} \log(E_0/A)$. However, a change of the primary composition is directly reflected in the elongation rate through

$$D_{10} = D_{10}^{\text{had}} \left(1 - \frac{d\langle \ln A \rangle}{d \log E} \right) \quad (16.26)$$

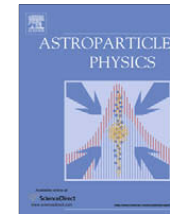
In general, in the presence of rising cross sections and violation of Feynman scaling as observed at colliders, the inelasticity of interactions increases with energy. As a consequence, the elongation rate of hadronic showers is always smaller than that of electromagnetic showers. Hence, observing an elongation rate similar or larger than 85 g/cm^2 is a very strong indication of a change of the mass composition toward a lighter mix of primary particles.

16.6 Shower universality and cross section measurement

By the 1980s Hillas had already pointed out that electromagnetic showers exhibit universality features [527]. The prediction of cascade theory for the mean longitudinal profile of EM showers being only a function of shower age s can be extended to individual showers. By introducing the empirical definition of shower age

$$s = \frac{3}{1 + 2X_{\max}/X}, \quad (16.27)$$

each individual shower profile can be considered as function of this age parameter. As simulations show, the normalized shower profiles are reasonably well described by a single universal profile, independent of primary energy and even of the mass composition [528, 529]. The origin of this universality lies in the nature of the cascade process for large particle numbers and is related to particle multiplication and absorption reaching an equilibrium at shower maximum, washing out any initial fluctuations [530]. For high-energy showers ($E \gtrsim 10^{17}$ eV), essentially all relevant quantities of shower particles such as energy, angle and time distributions can be parametrized as functions of shower age and lateral distance scaled by the Molière unit [504, 531]. Such parametrizations are particularly useful for estimating the Cherenkov light contribution [532] to the shower signal measured with fluorescence telescopes. Very powerful shower reconstruction methods can be developed by employing universality features to obtain an effective multivariate analysis of all observables [533].



Universality of electron–positron distributions in extensive air showers

S. Lafebre^{a,*}, R. Engel^b, H. Falcke^{a,c}, J. Hörandel^a, T. Huege^b, J. Kuijpers^a, R. Ulrich^b

3. Longitudinal description

There are several ways to describe the longitudinal evolution of an air shower.

Slant depth X measures the amount of matter an air shower has traversed in the atmosphere, in g/cm^2 .

Relative evolution stage is defined here in terms of the depth relative to the slant depth X_{max} , where the number of particles in the air shower reaches its maximum

$$t \equiv \frac{X - X_{\text{max}}}{X_0}, \quad (1)$$

with $X_0 \simeq 36.7 \text{ g}/\text{cm}^2$ being the radiation length of electrons in air. Because the shower maximum always lies at $t = 0$, describing multiple showers in terms of this quantity rather than X is expected to lead to a higher degree of universality.

Shower age is defined here so that $s = 0$ at the top of the atmosphere, $s = 1$ at the shower maximum, and $s = 3$ at infinite depth

$$s \equiv \frac{3X}{X + 2X_{\text{max}}} = \frac{t + X_{\text{max}}/X_0}{t/3 + X_{\text{max}}/X_0}. \quad (2)$$

The concept of shower age arises naturally from cascade theory in purely electromagnetic showers [3,27].

4. Energy spectrum

From cascade theory, the energy spectrum of electrons and positrons as a function of shower age takes an analytical form as derived by Rossi and Greisen [3]; a thorough previous study of this parameterization was done by Nerling et al. [10]. Loosely translating this description in terms of t , we replace the equation by

$$n(t; \ln \epsilon) = \frac{A_0 \epsilon^{\gamma_1}}{(\epsilon + \epsilon_1)^{\gamma_1} (\epsilon + \epsilon_2)^{\gamma_2}}, \quad (6)$$

where ϵ is the energy of a given secondary particle in the shower, and $\epsilon_{1,2}$ depend on t . We have performed a fit to this function for electrons, positrons and their sum, indirectly providing a description of the negative charge excess of extensive air showers as a function of evolution stage and secondary energy. In these fits the exponent γ_1 was fixed at $\gamma_1 = 2$ for positrons and $\gamma_1 = 1$ for both electrons and the total number of particles. The parameters for all three cases are explained in Appendix A.1.

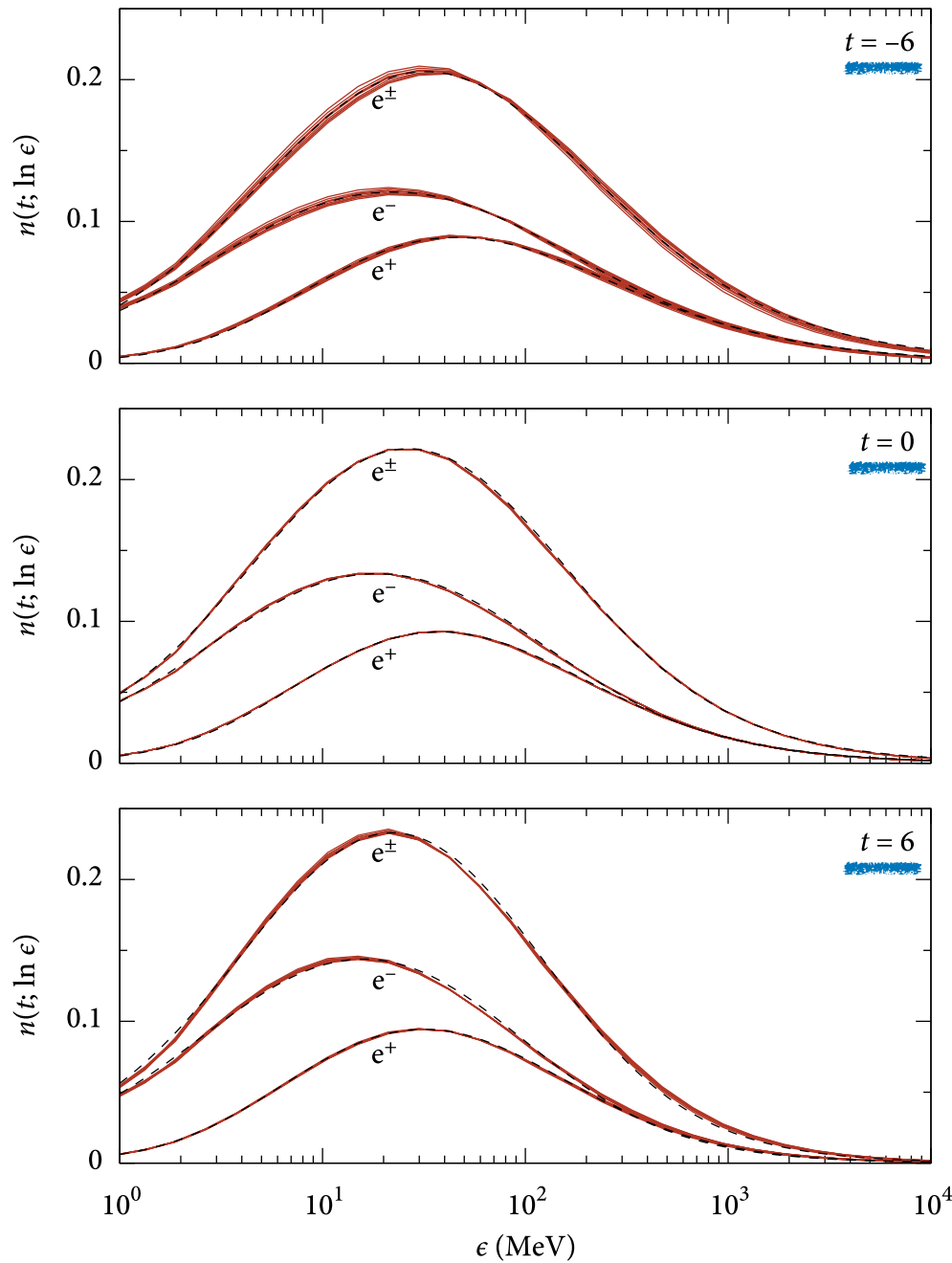


Fig. 2. Average energy distribution for different evolution stages $t = -6, 0, 6$ for electrons (marked e^-), positrons (e^+), and their sum (e^\pm). Background curves represent simulated distributions for different primaries (p, Fe, and γ) and energies (10^{17} , 10^{18} and 10^{19} eV). The corresponding parameterized distributions from (6) are plotted on top (dashed).

5. Angular spectrum

The angular distribution of particles is an important factor for observations with Cherenkov and radio telescopes. For successful radio detection an antenna needs to be placed close to the shower impact position, because geosynchrotron radiation is beamed in a very narrow cone in the direction of propagation [33]. As far as the particle distributions are concerned, the size of the patch that is illuminated on the ground then depends on the lateral distribution of the particles (cf. Section 7) and the angle with respect to the shower axis at which they propagate. Likewise, for Cherenkov observations the angle at which photons are emitted is a convolution of the density-dependent Cherenkov angle, which is of the order of $\sim 1^\circ$, and the angular distribution of the particles that emit them.

To compensate for the increase in solid angle with rising θ , the distribution of vertical momentum angles plotted here is defined in terms of Ω as

$$n(t; \ln \epsilon, \Omega) = \frac{n(t; \ln \epsilon, \theta)}{\sin \theta}.$$

(7)

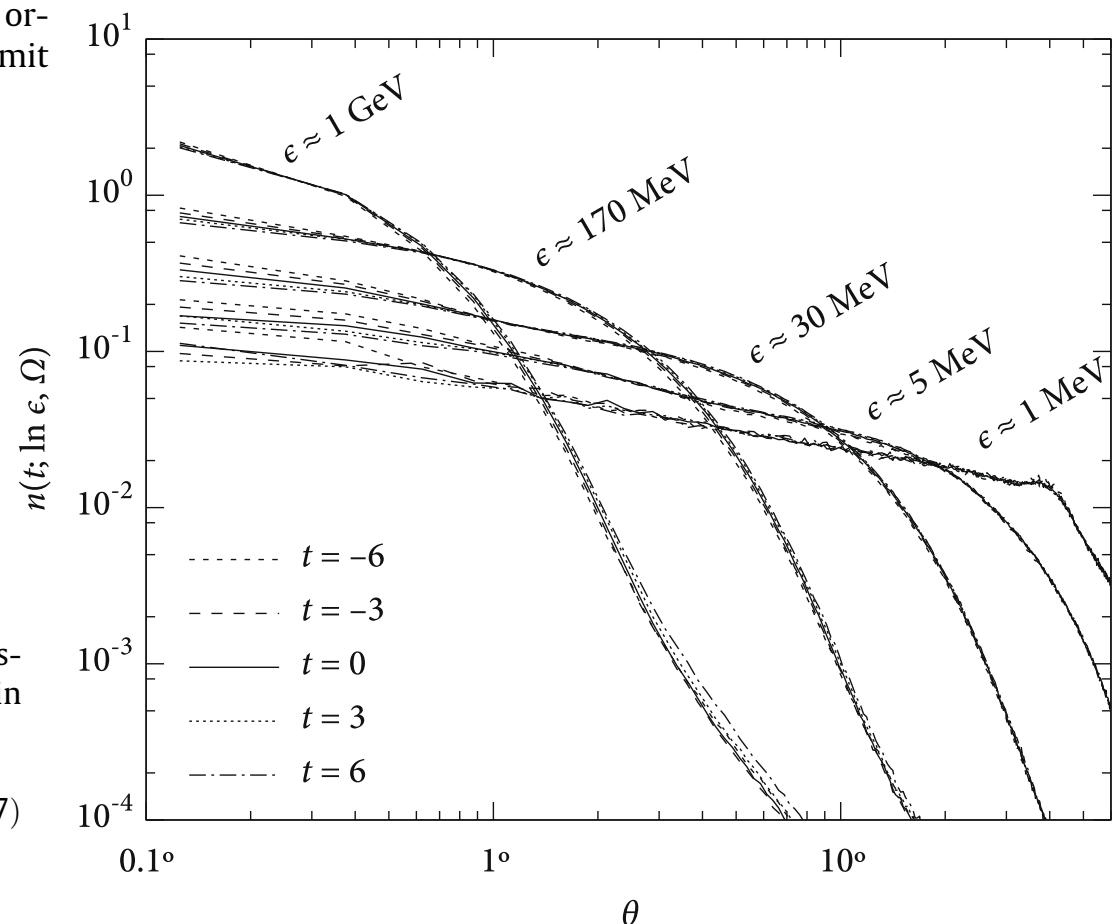


Fig. 4. Normalized average distributions $n(t; \ln \epsilon, \Omega)$ for different shower stages, averaged over 20 proton-initiated showers at 10^{18} eV.

The universality with respect to t allows us to parameterize this distribution as a function of two physical quantities only: momentum angle and energy. We propose the form

$$n(t; \ln \epsilon, \Omega) = C_0 \left[(e^{b_1 \theta^{\alpha_1}})^{-1/\sigma} + (e^{b_2 \theta^{\alpha_2}})^{-1/\sigma} \right]^{-\sigma}, \quad (8)$$

to describe the distribution. Values for α_i and b_i , which envelop the dependence on ϵ , are chosen such that the first term describes the flatter portion of the angular distribution parallel to the shower axis and the second represents the steep drop. The value of σ determines the smoothness of the transition from the flat region to the steep region. Best fit values for σ , b_i , and α_i are given in [Append](#)

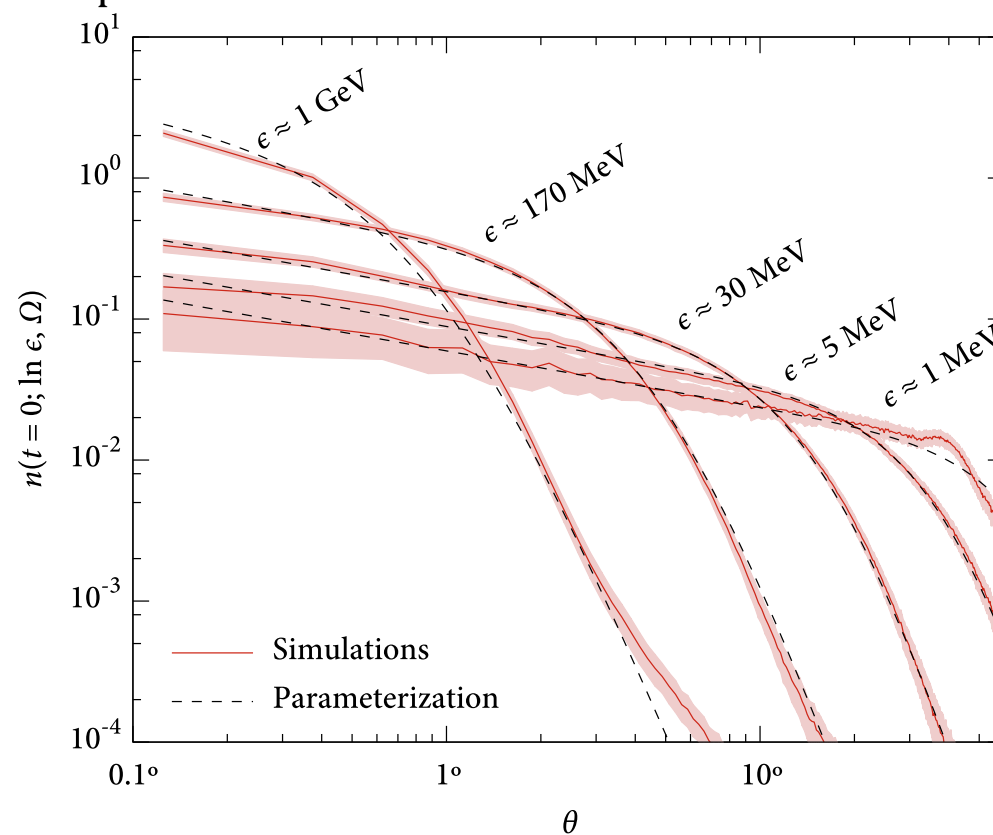


Fig. 5. Normalized average electron distributions $n(t = 0; \ln \epsilon, \Omega)$ (solid) for 20 proton showers at 10^{18} eV with 3σ statistical error margins (filled area). For each energy, corresponding parameterizations according to (8) are also drawn (dashed).

7. Lateral distribution

The lateral spread of particles in an air shower is of direct relevance since it is the primary means of obtaining information about the shower in ground-based scintillator experiments measuring particle densities at different lateral distances. By integrating the measured distribution or using the particle density at a given distance, an estimate for the primary energy can be made. Exact knowledge of the lateral distribution shape is therefore crucial to accurately determine the shape of the cosmic-ray energy spectrum.

When looking at the lateral distribution of electron and positrons in terms of the lateral distance r from the shower axis, a very poor level of universality is encountered. This is mainly due to differences in atmospheric density at the individual values of X_{\max} . We can compensate for these differences by expressing the lateral distance in terms of the Molière unit r_M , defining [35]

$$x \equiv \frac{r}{r_M} \simeq \frac{r \rho_A(h)}{9.6 \text{ g/cm}^2}, \tag{11}$$

where $\rho_A(h)$ is the atmospheric density as a function of height h . For different values of ϵ , the normalized lateral particle distribution at $t = 0$ is shown in Fig. 9 as a function of distance for 20 individual proton showers. In this figure, all curves line up as the compensation for density is applied. Note that the physical density $N(t; r)$, expressed in particles per unit area, is proportional to $N(t; \ln x)/x^2$:

$$N(t; \ln x) = \frac{\partial N(t)}{\partial \ln x} = 2\pi x^2 r_M^2 \frac{\dot{N}(t)}{2\pi r dr}, \tag{12}$$

and decreases strictly with distance from the shower axis. As expected, particles with higher energies tend to remain closer to the shower axis. This agrees with the observation that the angle of their momentum to the shower axis is smaller.

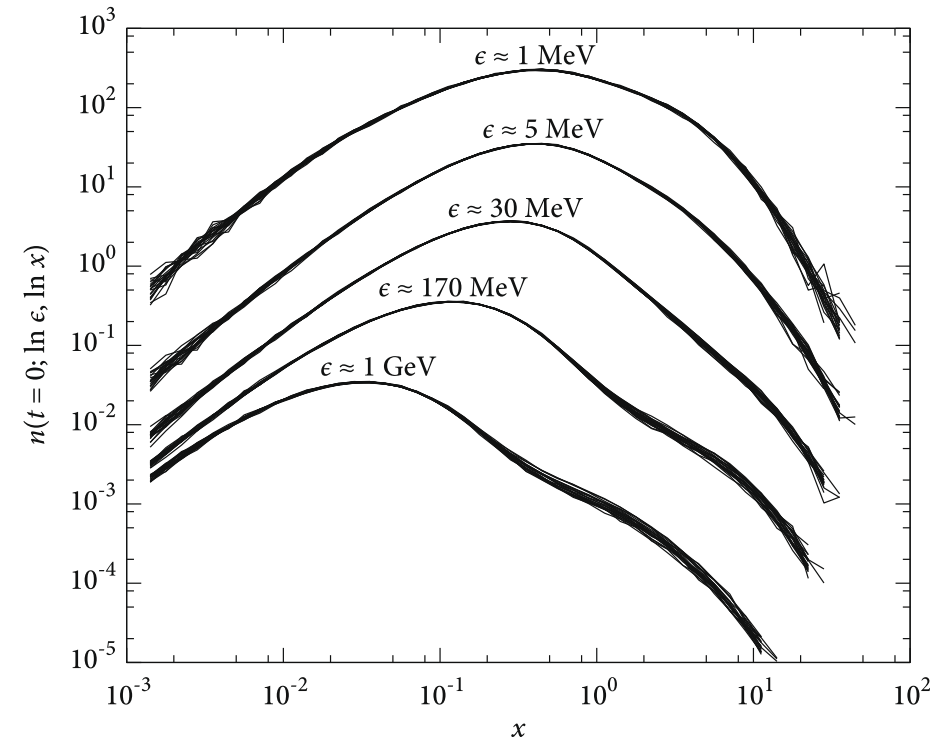


Fig. 9. Electron distributions $n(t = 0; \ln \epsilon, \ln x)$ for different electron energies as a function of distance to the shower axis for 20 individual showers initiated by 10^{18} eV protons. The curve set for 1 GeV is at the actual level; consecutive sets are shifted up by a factor of 10.

There is no statistically relevant dependence of the lateral distribution on zenith angle of incidence, nor does it change when electrons or positrons are considered separately, except at energies $\epsilon < 10\text{ MeV}$. There is, however, a significant effect with shower stage as shown in Fig. 10: older showers tend to be wider at the same secondary energy. Therefore, unlike in the case of angular distributions, in any parameterization of the lateral distribution a dependence on t must be incorporated. There is also a minor effect of the energy of the primary on the distribution, but this is only appreciable for secondary energies of $\epsilon > 1\text{ GeV}$.

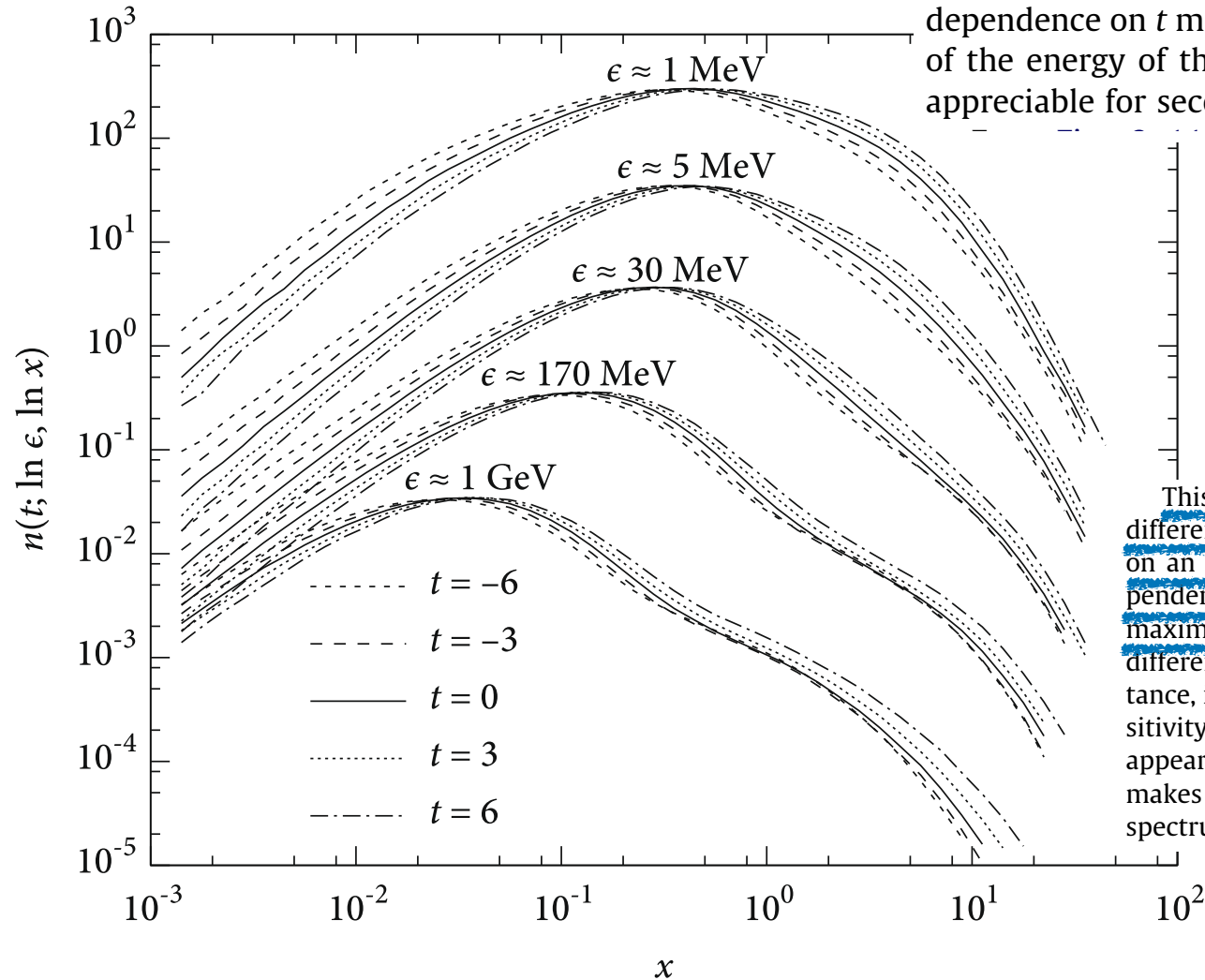


Fig. 10. Average distributions $n(t; \ln \epsilon, \ln x)$ for different shower stages, averaged over 20 proton-initiated showers at 10^{18} eV , clearly showing dependence on t . Again, consecutive sets are shifted up by a factor of 10.

This observation raises the question whether one could use this difference in lateral distribution to differentiate between primaries on an individual shower basis by their lateral distribution, independently of measurements of primary energy or depth of shower maximum. This would be a difficult task. First of all, appreciable difference in density only occurs at high energies and at some distance, implying that the total electron density in the region of sensitivity would be very small. Additionally, the effect does not appear at the same distance for different electron energies. This makes the feature less pronounced when an integrated energy spectrum is measured.

Traditionally, the integral lateral electron distribution is described by an approximation of the analytical calculation of the lateral distribution in electromagnetic cascades, the Nishimura–Kamata–Greisen (NKG) function [36,37]. The integral lateral distribution for our simulated set of showers $n(t; \ln x) \propto x^2 \rho_{\text{nkg}}$ is reproduced well by a parameterization of this form, provided that we allow the parameters to be varied somewhat. Let us define

$$n(t; \ln x) = C_2 x^{\zeta_0} (x_1 + x)^{\zeta_1} \quad (13)$$

as parameterization. In the original definition, described in terms of shower age s , we have $\zeta_0 = s$, $\zeta_1 = s - 4.5$, and $x_1 = 1$. Our simulated lateral spectra closely follow the values $\zeta_0 = 0.0238t + 1.069$, $\zeta_1 = 0.0238t - 2.918$, and $x_1 = 0.430$ to an excellent level for $10^{-3} < x < 10$.

proton-air cross section

One application of shower universality is the measurement of the proton–air cross section with air showers. The depth of the first interaction point of a shower is exponentially distributed

$$\frac{dP}{dX_1} = \frac{1}{\lambda_{\text{int}}} e^{-X_1/\lambda_{\text{int}}}, \quad (16.28)$$

where λ_{int} is the interaction length, which is related to the particle production cross section σ_{prod} (see Eq. 4.82) by $\lambda_{\text{int}} = \langle m_{\text{air}} \rangle / \sigma_{\text{prod}}$. It is, however, impossible to measure the early, low-multiplicity part of the shower development well enough to infer X_1 directly. Auxiliary quantities such as the depth of shower maximum, X_{max} , have to be used to derive information on the first interaction point. Indeed, the distribution of X_{max} is approximately exponential as expected from (16.28). The slope of this distribution, Λ , has to be converted to λ_{int} with detailed shower and detector simulations due to the importance of fluctuations. Simulations indicate that $\sim 50\%$ of the size of the shower-to-shower fluctuations of X_{max} of proton showers are due to the fluctuations of the first interaction point, for which we have $\text{RMS}(X_1) = \lambda_{\text{int}}$.

In addition to the need for correcting for shower-to-shower fluctuations, cross section measurements are also subject to uncertainties arising from the unknown primary mass composition. Typically showers with very deep X_{\max} are selected to suppress the contamination by heavier primaries.

A compilation of p -air cross section measurements is shown in Figure 16.4. The low-energy data are from experiments measuring the attenuation of the hadron flux in the atmosphere and the high-energy results are based on air shower measurements in combination with universality assumptions; see [535] for an overview of the different measurement methods, where also the references to the original work are given.

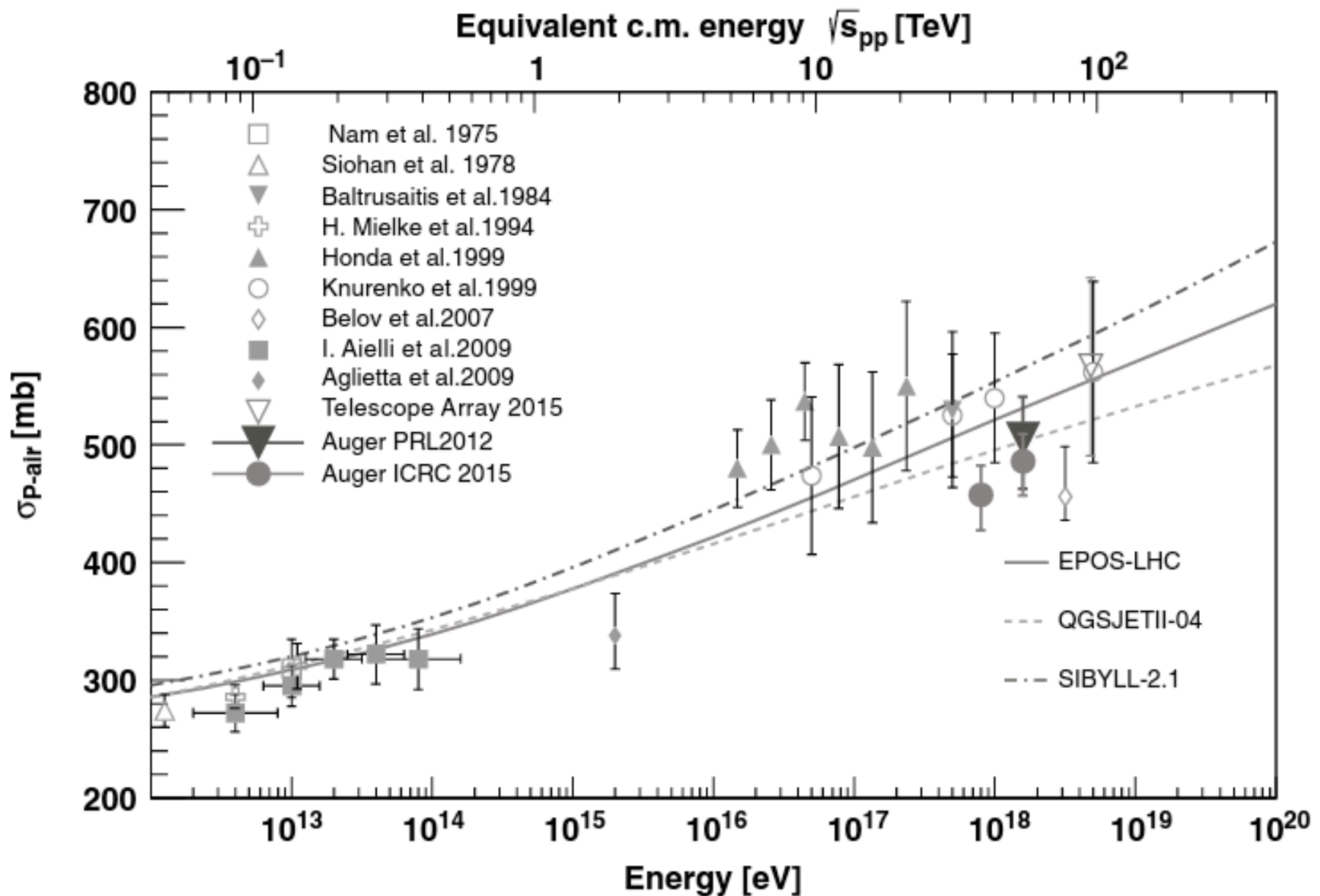


Figure 16.4 Proton–air cross section measured with cosmic ray experiments. The data are compared to predictions of hadronic interaction models. From Ref. [534], where also the references to the data and models are given.

Measurement of the Proton-Air Cross Section at $\sqrt{s} = 57$ TeV with the Pierre Auger Observatory

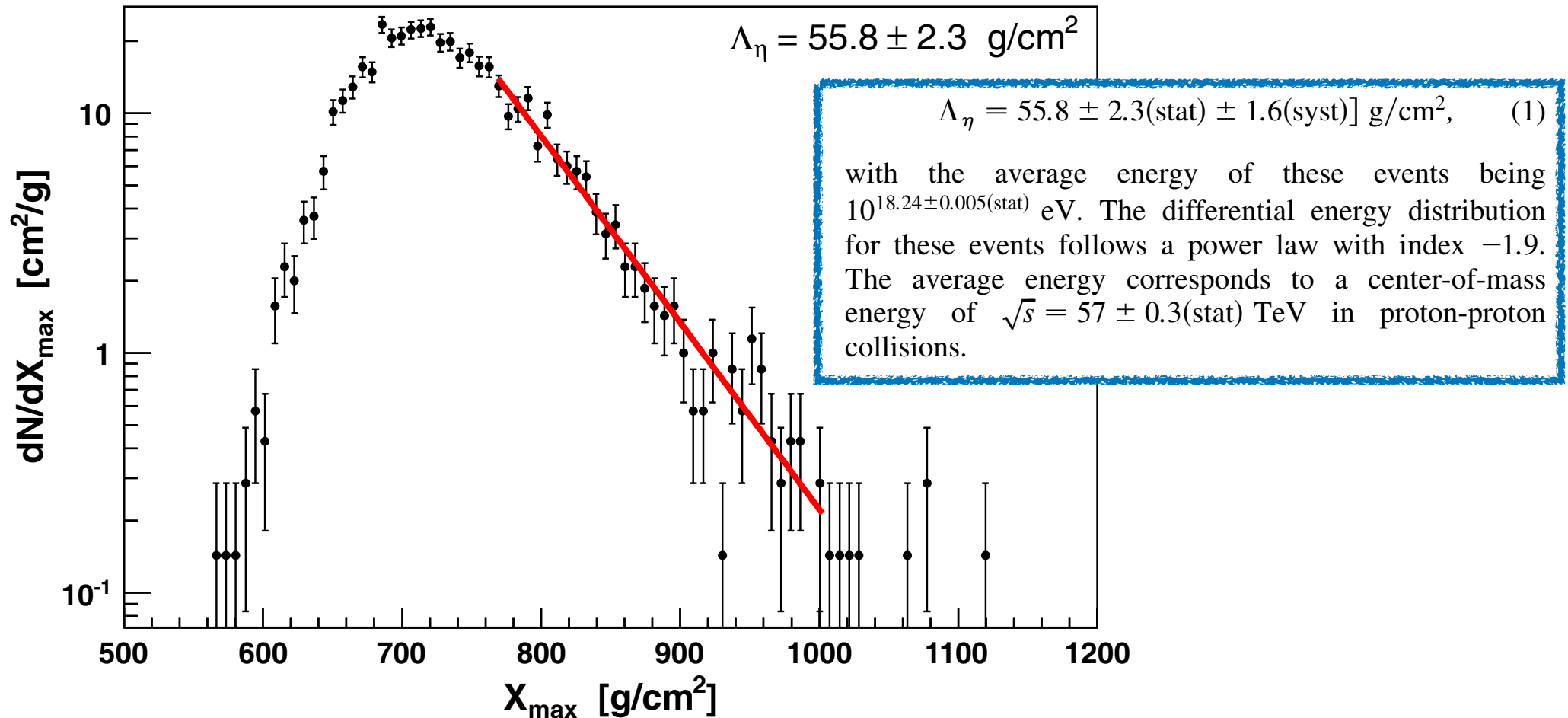


FIG. 1 (color online). Unbinned likelihood fit to obtain Λ_η (thick line). The X_{max} distribution is unbiased by the fiducial geometry selection applied in the range of the fit.

Determination of the cross section.—The determination of the proton-air cross section for particle production requires the use of air-shower simulations, which inherently introduces some dependence on model assumptions. We emulate the measurement of Λ_η with Monte Carlo simulations to derive predictions of the slope, Λ_η^{MC} . It is known from previous work that the values of Λ_η^{MC} are directly linked to the hadronic cross sections used in the simulations [2]. Accordingly we can explore the effect

Ultrahigh-energy cross section from study of longitudinal development of air showers

R. W. Ellsworth

Department of Physics, George Mason University, Fairfax, Virginia 22030

T. K. Gaisser and Todor Stanev*

Bartol Research Foundation of The Franklin Institute, University of Delaware, Newark, Delaware 19711

G. B. Yodh

Department of Physics, University of Maryland, College Park, Maryland 20742

(Received 1 March 1982)

We present calculations of the type that will be necessary for interpretation of large cosmic-ray experiments that measure longitudinal profiles of individual showers. A primary goal of such experiments is to determine both cross section and composition around 10^{18} eV.

Even without the problem of heavy primaries, measurement of x_m or $x_{1/4}$ alone cannot determine an arbitrarily large proton cross section because of intrinsic fluctuations in shower development. The results of our calculations bear this out, as shown in Fig. 2. Here we show Λ_m for proton showers only, as a function of $\sigma_{p\text{-air}}$ at 3×10^{17} eV. For the atmosphere,

$$\lambda_{p\text{-air}} \text{ (g/cm}^2\text{)} = \frac{2.4 \times 10^4}{\sigma_{p\text{-air}} \text{ (mb)}} .$$

We emphasize that Fig. 2 cannot at present be used for an accurate determination of $\sigma_{p\text{-air}}$ from Λ_m because of the dependence on composition mentioned above. In addition, possible effects of uncertainties in the interaction model and of instrumental fluctuations need to be understood.

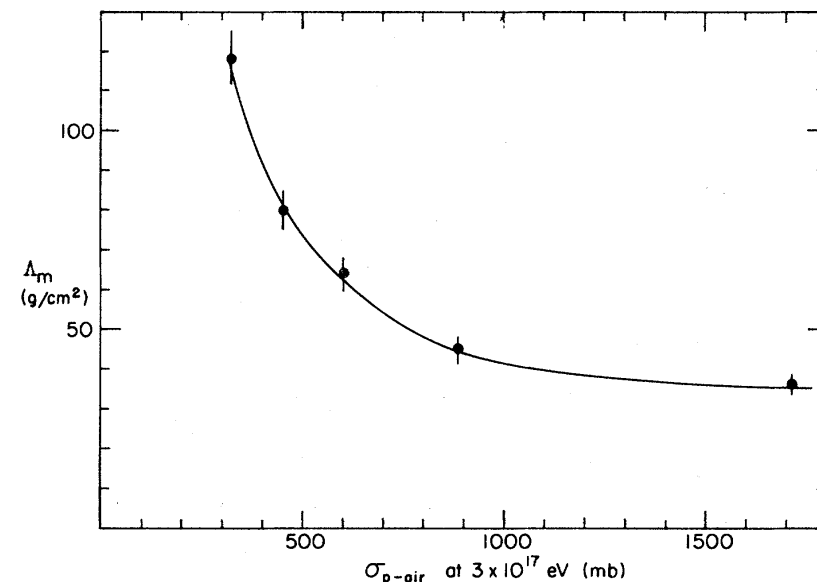


FIG. 2. Λ_m vs $\sigma_{p\text{-air}}$ for proton showers chosen from a power-law energy spectrum (differential index = 2) with $E_0 > 3 \times 10^{17}$ eV. Error bars show statistical uncertainty from the simulation result. Since the figure shows proton showers only, it cannot be used for an accurate determination of σ . See text.

Measurement of the Proton-Air Cross Section at $\sqrt{s} = 57$ TeV with the Pierre Auger Observatory

$$\sigma_{p\text{-air}}^{\text{prod}} = [505 \pm 22(\text{stat})_{-36}^{+28}(\text{syst})] \text{ mb}$$

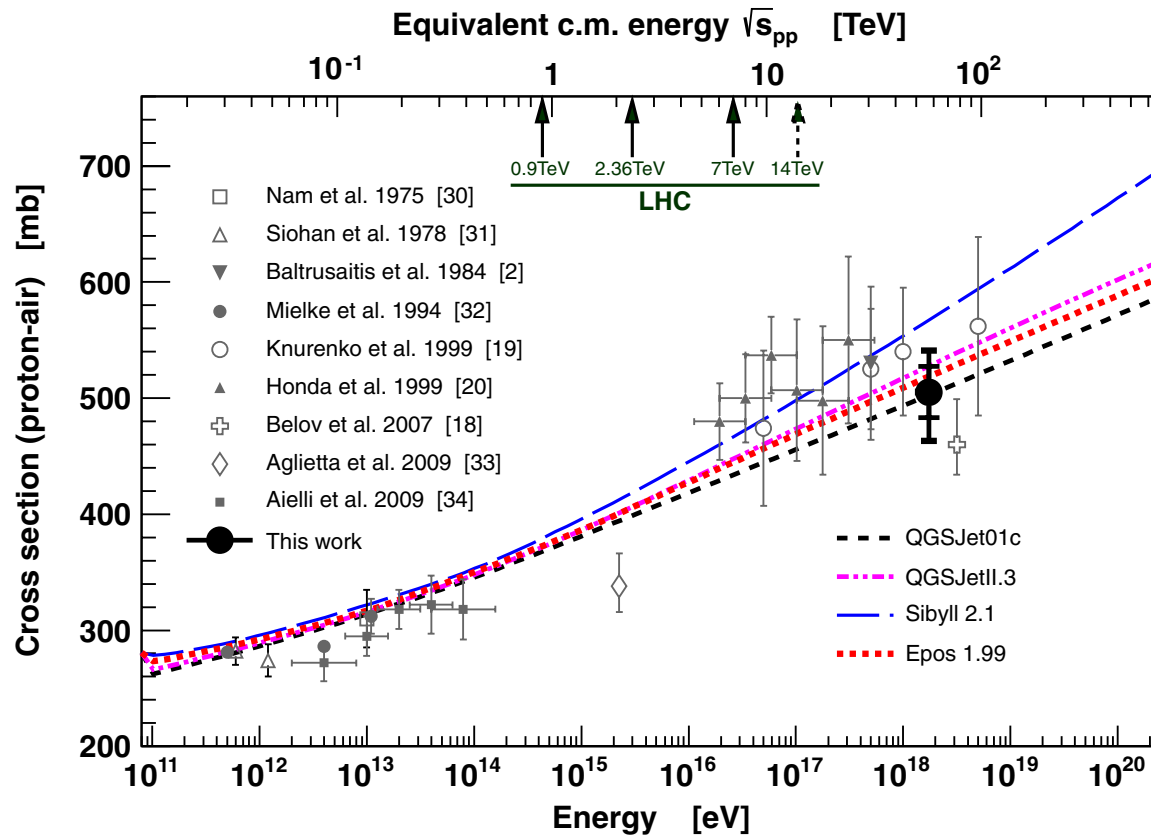


FIG. 2 (color online). Resulting $\sigma_{p\text{-air}}^{\text{prod}}$ compared to other measurements (see [18–20,30–34]) and model predictions. The inner error bars are statistical, while the outer include systematic uncertainties for a helium fraction of 25% and 10 mb for the systematic uncertainty attributed to the fraction of photons.

TABLE I. Summary of the systematic uncertainties.

Description	Impact on $\sigma_{p\text{-air}}^{\text{prod}}$
Λ_η systematics	± 15 mb
Hadronic interaction models	$-8 + 19$ mb
Energy scale	± 7 mb
Conversion of Λ_η to $\sigma_{p\text{-air}}^{\text{prod}}$	± 7 mb
Photons, $<0.5\%$	$< + 10$ mb
Helium, 10%	-12 mb
Helium, 25%	-30 mb
Helium, 50%	-80 mb
Total (25% helium)	-36 mb, $+28$ mb

Comparison with accelerator data.—For the purpose of making comparisons with accelerator data we calculate the inelastic and total proton-proton cross sections using the Glauber model. We use standard Glauber formalism [21],

This Glauber calculation is model-dependent since neither the parameters nor the physical processes involved are known accurately at cosmic-ray energies. In particular, this applies to the elastic slope parameter, B_{el} (defined by $d\sigma_{el}/dt \propto \exp(-|t|B_{el})$ for very small t), the correlation of B_{el} to the cross section, and the cross section for diffractive dissociation. For the example of σ_{pp}^{inel} , the correlation of B_{el} with the cross section is shown in Fig. 3 for $\lambda = 0.5$. We have used the same four hadronic interaction models to determine the uncertainty band of the B_{el} - σ_{pp}^{inel} correlation. Recent cross-section models such as [23] fall

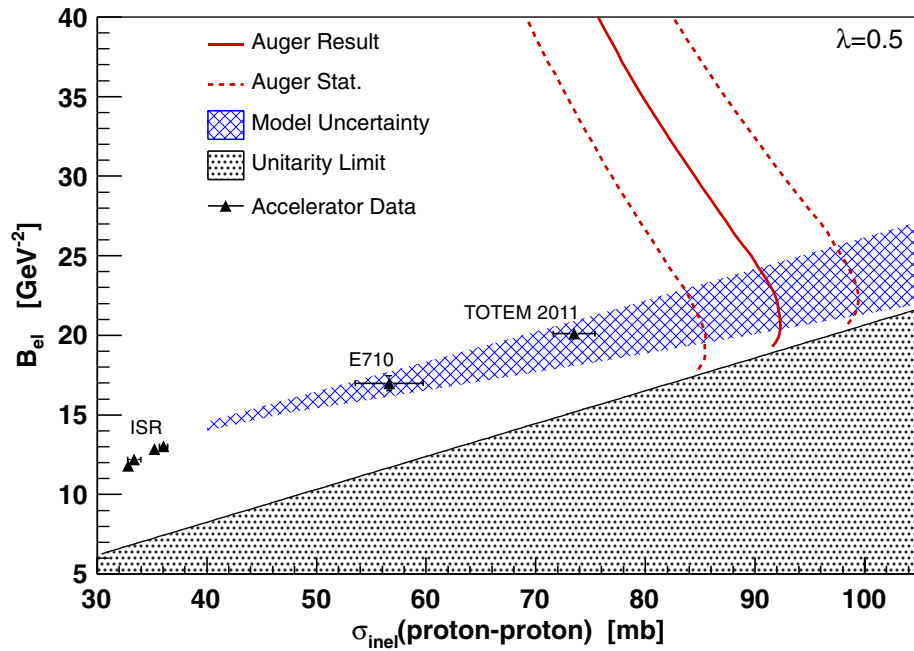


FIG. 3 (color online). Correlation of elastic slope parameter, B_{el} , and the inelastic proton-proton cross section in the Glauber framework. The solid line indicates the parameter combinations yielding the observed proton-air production cross section, and the dotted lines are the statistical uncertainties. The hatched area corresponds to the predictions by SIBYLL, QGSJET, QGSJETII, and EPOS. See also Ref.[5].

Measurement of the Proton-Air Cross Section at $\sqrt{s} = 57$ TeV with the Pierre Auger Observatory

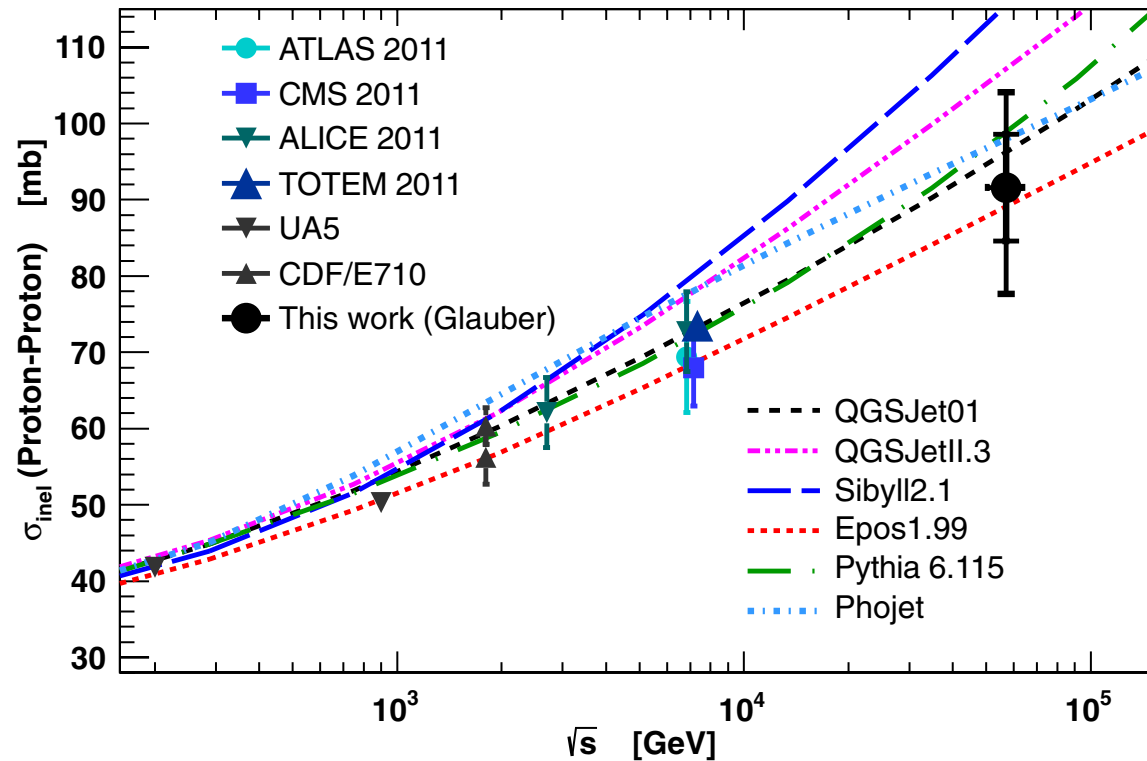


FIG. 4 (color online). Comparison of derived $\sigma_{pp}^{\text{inel}}$ to model predictions and accelerator data [29]. Here we also show the cross sections of two typical high-energy models, PYTHIA6 [35] and PHOJET [36]. The inner error bars are statistical, while the outer include systematic uncertainties.

We find that in the Glauber framework the *inelastic* cross section is less dependent on model assumptions than the *total* cross section. The result for the inelastic proton-proton cross section is

$$\sigma_{pp}^{\text{inel}} = [92 \pm 7(\text{stat})_{-11}^{+9}(\text{syst}) \pm 7(\text{Glauber})] \text{ mb},$$

and the total proton-proton cross section is

$$\sigma_{pp}^{\text{tot}} = [133 \pm 13(\text{stat})_{-20}^{+17}(\text{syst}) \pm 16(\text{Glauber})] \text{ mb}.$$

The systematic uncertainties for the inelastic and total cross sections include contributions from the elastic slope parameter, from λ , from the description of the nuclear density profile, and from cross-checking these effects using QGSJETII [9,24]. For the inelastic case, these three independent contributions are 1, 3, 5, and 4 mb, respectively. For the total cross section, they are 13, 6, 5, and 4 mb. We emphasize that the total theoretical uncertainty of converting the proton-air to a proton-proton cross section may be larger than estimated here within the Glauber model.